Cerebellar contributions to a brainwide network for flexible behavior

Jessica L. Verpeut[1**], Silke Bergeler[1,2,3], Mikhail Kislin[1], F. William Townes[4], Ugne Klibaite[5], Zahra M. Dhanerawala[1], Austin Hoag[1], Caroline Jung[1], Junuk Lee[1], Thomas J. Pisano[1], Kelly M. Seagraves[1], Joshua W. Shaevitz[2,3], Samuel S.-H. Wang[1**]

[1]Neuroscience Institute, Washington Road, Princeton University, Princeton, NJ 08544 USA.
[2]Department of Physics, Princeton University, Princeton, NJ 08544 USA.
[3]Lewis-Sigler Institute for Integrative Genomics, Princeton University, Princeton, NJ 08544 USA.
[4]Department of Computer Science, Princeton University, Princeton, NJ 08544 USA.
[5]Department of Organismic and Evolutionary Biology, Harvard University MA, 01451 USA.

**Corresponding authors

Correspondence: Samuel S.-H. Wang
Neuroscience Institute, Washington Road
Princeton University
Princeton, New Jersey 08544 USA
sswang@princeton.edu
+1 (609) 258-0388

Jessica Verpeut
Department of Psychology
Arizona State University
950 South McAllister Avenue
Tempe, Arizona 85281 USA
jverpeut@asu.edu
+1 (480) 727-5052

Keywords: cerebellum, cognitive, flexible behavior, light-sheet microscopy, mouse, reversal learning, Purkinje cells, c-Fos, whole brain

Significance statement

The cerebellum, part of all vertebrate brains, adjusts action on a split-second basis in response to unexpected events. Adjustments can range from minute movements to broad changes in behavior. In mice, we investigated cerebellar regions that help guide flexible behavior. Inactivation of these regions prevented mice from responding flexibly to a changing Y-shaped maze. We used light-sheet microscopy of protein expression to map brainwide effects of cerebellar inactivation. Inactivation caused changes in thalamus and neocortex that were similar in pattern, but opposite in sign, from normal learning. The same inactivation also impaired multiday adaptation to an open arena, tracked using machine vision. Our work shows how the cerebellum's influence over nonmotor action can be mediated by a widespread brain network.

Abstract

The cerebellum regulates nonmotor behavior, but the routes by which it exerts its influence are not well characterized. Here we report a necessary role for posterior cerebellum in guiding flexible behavior, acting through a network of diencephalic and neocortical structures. After chemogenetic inhibition of Purkinje cells in lobule VI or crus I, high-throughput automated analysis of complex whole-body movement revealed deficiencies in across-day adaptation to an open field environment. Neither perturbation affected gait, within-day open-field adaptation, or location preference. Mice could learn a water Y-maze task but were impaired in their ability to reverse their initial choice. To map targets of perturbation, we imaged c-Fos activation in cleared whole brains using light-sheet microscopy. Reversal learning activated diencephalic regions and associative neocortical regions. Distinctive subsets of structures were altered by perturbation of lobule VI (thalamus and habenula) and crus I (hypothalamus and prelimbic/orbital cortex), and both perturbations influenced anterior cingulate and infralimbic cortex. Taken together, these experiments reveal parts of a brainwide system for cerebellar influence to guide flexible learning.

Introduction

A recently appreciated contributor to flexible behavior is the cerebellum, a structure better known for its role in shaping movement and balance. Prominent anatomical pathways between cerebellum and neocortex suggest a role in higher-order processing (De Zeeuw, 2021; De Zeeuw et al., 2021; Leiner et al., 1993, 1986; Pisano et al., 2021). Insult to the posterior cerebellum results in a clinical cognitive-affective syndrome that includes impairments in executive function, working memory, abstract reasoning, and emotional processing (Schmahmann, 2013; Schmahmann and Sherman, 1998). More severe outcomes arise from pediatric cerebellar insult, including a diagnosis of autism, a disorder characterized by inflexibility to the point of emotional distress when routines are violated (Fatemi et al., 2012; Latinus et al., 2019; Limperopoulos et al., 2014, 2010; Uddin et al., 2015; Wang et al., 2014). Taken together, these studies suggest that, like the neocortex, the cerebellum plays a necessary role in flexible behavior and cognitive processing.

Animal experiments have identified specific regions of the cerebellar cortex that support flexible behavior. In lobule VI, a midline posterior structure that is perturbed in autism spectrum disorder (Crucitti et al., 2020; Traut et al., 2018), inhibition of molecular layer interneurons alters reversal learning, perseverative or repetitive behavior, novelty-seeking, and social preference (Badura et al., 2018). Disruption of right crus I, which is also perturbed in ASD, leads to deficits in social, repetitive, and flexible behaviors but does not affect gait (Badura et al., 2018; Stoodley et al., 2017). Furthermore, inactivation of Purkinje cells in crus I reduces the ability to perform sensory evidence accumulation, a task in which Purkinje cells have been found to encode choices and accumulated evidence (Deverett et al., 2019, 2018).

Lobule VI and crus I engage with the forebrain through bidirectional polysynaptic pathways (Strick et al., 2009). Purkinje cells in the cerebellar cortex receive input from distal forebrain

structures and send inhibitory output to cerebellar and vestibular nuclei, which in turn provide excitatory output to the rest of the brain forming the cerebral-thalamic-cerebellar circuit (De Zeeuw, 2021; De Zeeuw et al., 2021; Eccles et al., 1966; Kelly and Strick, 2003; Leiner et al., 1993, 1986). Along these pathways, cerebellar cortex is organized into parasagittal microzones which project in distinctive patterns, so that lobule VI and crus I make different patterns of disynaptic connectivity with thalamic structures (Andersson and Oscarsson, 1978; Apps and Hawkes, 2009; Gravel and Hawkes, 1990). Trisynaptic tracing from these cerebellar regions leads to anterior cingulate, infralimbic, and somatosensory cortex (De Zeeuw, 2021; De Zeeuw et al., 2021; Leiner et al., 1993, 1986; Pisano et al., 2021).

To interrogate the contribution of the posterior cerebellum to flexible behavior, we monitored mouse behavior and mapped brain-wide patterns of activation after perturbing lobule VI and crus I. First, we chemogenetically perturbed neural activity reversibly in Purkinje cells, the principal output neurons of the cerebellar cortex. Second, we characterized freely-moving mouse behavior in granular detail using machine learning methods for automated tracking of body poses, movements, and actions. Third, we combined a Y-maze learning paradigm with c-Fos mapping to identify brain-wide substrates of reversal learning. Lastly, we studied expression of the activity-dependent gene product c-Fos using tissue clearing techniques combined with light-sheet microscopy to map the whole brain without need for tissue sectioning. Together, these approaches provide a framework for characterizing how the cerebellum modulates flexible behavior.

Results

Experimental design to reversibly perturb Purkinje cells

To probe the impact of cerebellar activity on flexible behavior and whole-brain activity, we chemogenetically inhibited Purkinje cells. Purkinje cells influence the rest of the brain via their projections to the deep cerebellar nuclei (DCN), which send excitatory output to the rest of the brain. The inhibitory DREADD (Designer Receptor Exclusively Activated by Designer Drugs) hM4Di was expressed in Purkinje cells using an adeno-associated virus (AAV) containing the hM4Di sequence under control of the L7 promoter. DREADD expression was robust and confined to Purkinje cells (**Figure 1A; Figure 1-figure supplement 1A-C**). In slices, application of the DREADD agonist clozapine-N-oxide (CNO; 10 µM) reduced evoked action potential firing in hM4Di-positive Purkinje cells in slices (paired t-test, p = 0.0009) (**Figure 1B-D**), thus removing modulation of DCN neurons. To test the consequences for deep-nuclear firing, we made many-electrode recordings in 5 awake mice and identified a total of 43 units in which tactile airpuff stimuli evoked at least a 5 Hz facilitation increase in firing (**Figure 1E-G; Figure 1-figure supplement 2**). In these units, application of CNO increased spontaneous firing rates (-10: 32.5 Hz, SD: 17.6; 20: 36.8 Hz, SD: 18.9; 50: 39 Hz, SD: 22.5; paired t-test: p = 0.033 -10 vs 20 min, p = 0.013 20 vs 50 min) (**Figure 1F; Figure 1-figure supplement 2D**). Before CNO application, tactile airpuffs first evoked an increase in DCN activity during the airpuff, consistent with mossy-fiber and/or climbing-fiber drive, followed by a strong undershoot. Inhibition of Purkinje cells abolished the undershoot, leaving a sustained increase in firing that outlasted the duration of the airpuff, consistent with decreased spontaneous Purkinje cell drive and consequent increased feedback inhibition via the nucleo-olivary pathway. (-10: 32.5 +/- 17.6, 20: 36.8 +/-18.9, 50: 39 +/-22.5)

Posterior vermis (lobule VI and VII) and ansiform area (crus I and crus II) have been implicated in non-motor executive functions (**Figure 1H**) (Badura et al., 2018; Ozol et al., 1999; Reeber et al., 2012; Sillitoe et al., 2003). We stereotaxically injected virus into either lobule VI or crus I at postnatal day (PND) 56 and at sacrifice quantified mCherry-positive voxels (**Figure 1-figure supplement 1D**). We administered CNO (1 mg/kg intraperitoneal) on test days between PND 77 and PND 90 and tested animals on two paradigms for assessing flexible behavior: spontaneous behavior in an open-field arena, and reversal learning in a water Y-maze (**Table 1**). At different points of Y-maze training, we sacrificed mice and collected tissue for whole-brain imaging of the activity-dependent immediate early gene c-Fos (**Figure 1I**).

Lobule VI and crus I modulate multiday behavioral adaptation to an open field

To measure the capacity of mice to adapt to a novel environment, we characterized spontaneous behavior in an open-field arena (Klibaite et al., 2022). We recorded mouse behavior by imaging from beneath for 20 minutes over two days in order to track location and to allow automated tracking of body parts using the LEAP (LEAP Estimates Animal Pose) software package (Pereira et al., 2019), a neural network trained to track the positions of 18 joints (**Figure 2A; Figure 2B, movie supplement 1**).

We recorded animals for 20 minutes on each of two days, after a dose of CNO on day 1 and a dose of vehicle on day 2. Over successive days, control mice that did not receive AAV reduced their daily amount of locomotion (two-way mixed ANOVA $F(1,47) = 146$, $p < 0.001$). Disruption of lobule VI activity prevented this adaptation. Lobule VI-perturbed mice traveled significantly more on the second day ($d = 2.3$, one-way ANOVA $F(4,47) = 5.04$, $p = 0.002$, Dunnett post-hoc test $p < 0.001$) compared to the control group. The total distance traveled on day 2 was not significantly different from the distance on day 1 in lobule VI perturbed mice, in contrast to a

decrease for mice with a unilateral or bilateral disruption of crus I (*d* = 2.6, 2.4, and 1.4 for bilateral crus I, left crus I, and right crus I), or control mice (*d* = 3.4, repeated-measures ANOVA for each group, $p < 0.01$, Bonferroni correction) (**Figure 2A)**.

Perturbation of lobule VI or crus I did not change the fraction of time mice spent in the inner region of the open field arena compared to control animals on day 1. Right crus I-perturbed animals did spend a significantly larger fraction of time in the inner region of the open field arena on day 1 ($r = 0.6$, Kruskal-Wallis test chi-squared(4) = 9.52, $p = 0.049$, pairwise comparisons using Wilcoxon rank sum exact test $p = 0.02$, Benjamini-Hochberg correction) (**Figure 2- figure supplement 1A**). None of the manipulations affected locomotory gait (**Figure 2-figure supplement 1B**) or spatial preferences in the arena such as locomotion in the periphery and grooming in corners (**Figure 2-figure supplement 1D**).

To explore the structure of this altered behavior, we used automated pose analysis. We performed semi-supervised behavioral clustering on LEAP-tracked body-part locations to identify six clusters of body dynamics: slow exploration, grooming, fast exploration, rearing, turning walk, and locomotion. We took the clusters as behavioral states to generate an ethogram, arranged in order of increasing centroid speed (**Figure 2B**). Since mice spent the most time in locomotion, we further subdivided locomotion into three groups, slow, medium, and fast, based on centroid velocity (**Figure 2-figure supplement 1C**).

The fractions of time spent in each of the eight behaviors was significantly different for lobule VI-perturbed mice compared to the control animals. More specifically, compared with control animals, lobule VI disruption led to decreases in time spent in the rearing state on day 1 and increases in fast locomotion on day 2 (**Figure 2-figure supplement 2A-B, D**). The ratio of fast locomotion in lobule VI-perturbed mice compared to the control group on day 2 was 1.7, sufficient to account for the increased total distance traveled on day 2 compared to the other

groups. Within each day's 20 minutes of observation, the probability of being in the fast locomotion state decayed over time. However, lobule VI-perturbed, bilateral crus I-perturbed, and right crus I-perturbed mice were more likely to perform fast locomotion just after the experiment started on day 2 compared to day 1, in contrast to our observations for the control group and left crus I perturbation (**Figure 2C**).

We calculated complex adaptation as the ratio of time spent in each state for day 2 compared to day 1. Overall, the adaptation ratio was closer to 1 for lobule VI-perturbed mice for most behavioral states, especially fast locomotion and slow exploration (**Figure 2D; Figure 2-figure supplement 2D**). There were few differences between controls, but CNO exposed animals had a slight reduction in locomotion (**Figure 2-figure supplement 2C**). We next examined transition probabilities between behavioral states. In control animals, day 2 probabilities compared to day 1 showed higher transition frequencies in the direction of less-active states (*i.e.,* above the diagonal of the matrix in **Figure 2-figure supplement 1E**). This tendency was markedly reduced in lobule VI-treated animals. In crus-I perturbed mice, the same semi-supervised behavioral clustering analysis found subtle differences, in particular a right crus I-induced shift from fast-locomotion state to the slow-locomotion state starting on day 1 (**Figure 2D; Figure 2-figure supplement 2A-B**). In summary, lobule VI-perturbed animals maintained similar within-day response patterns to the same environment despite impaired adaptation over two days of exposure.

Cerebellar disruption of lobule VI or bilateral crus I impairs Y-maze reversal learning

To test flexible learning, we trained mice in a water Y-maze (**Figure 3A**). After 1 day of habituation to the environment, an underwater platform was placed at the end of one Y-arm and the mice spent two days learning to find the platform through trial and error (acquisition days 2 and 3). On

day 4, the platform was switched to the opposite arm for 4 sessions (reversal). On the fifth and final session on day 4, a barrier was placed blocking the originally learned side (forced reversal). On all days, we defined correct choice as an entrance to the correct arm and climbing onto the platform during the 40-second trial.

All DREADD-activated groups showed a similar time course of initial acquisition, showing no statistically detectable differences compared with controls (generalized linear mixed-effect model, GLMM, p=0.76; **Figure 3B**; for control experimental design, see **Methods**). Control treatments did not affect distance swum, initial learning, or reversal learning compared with untreated mice (**Figure 3-figure supplement 3A-D**). Lobule VI-perturbed mice and bilateral crus-I-perturbed mice were strongly impaired in reversal learning (**Figure 3C and Figure 3-figure supplement 3E**; lobule VI compared to CNO-without-DREADD controls $p = 8.9*10^{-06}$, Cohen's *d* = 3.84 and bilateral crus I p = 0.04, Cohen's *d* 1.93. Performance on the forced-reversal session was also reduced (lobule VI, p = 0.0039) (**movie supplement 2**). In tests for lateralization of crus I function (Tsai et al., 2018), we found that neither left- (p = 0.83) or right- (p = 0.10) crus-I-perturbed mice showed impaired reversal (**Figure 3C**).

To probe behavioral patterns of this learning failure, we analyzed individual trials. Entrance into any arm N times, ending with a landing in the correct arm, was defined as an N-th choice trial. Even in the first reversal session, control mice (CNO only) typically found the platform in their first or second choice (85% of mice), eventually making a correct first choice in 71% of trials by the fourth session. In contrast, lobule-VI-perturbed mice made persistent errors even by the fourth session, making correct first choices on 16% of trials and correct second choices on 34% of trials (**Figure 3D and Figure 3-figure supplement 3F**). In forced-reversal trials, lobule-VI-perturbed mice displayed a unique perseverative behavior of swimming back and forth between the divider and beginning of the maze instead of switching to the obvious open arm, resulting in animals failing to switch in 64% of forced-reversal trials (**movie supplement 2**). We also observed

perseveration in crus-I perturbed mice, whereby mice continued to swim to the previously correct arm and failed to switch in 47% of forced-reversal trials. (**Figure 3D, Figure 3-figure supplement 3F**). In summary, mice typically learned the Y-maze by trying multiple arms until the platform was found, but perturbing the cerebellum resulted in persistent errors and a failure to reverse.

Whole-brain c-Fos reveals lobule-specific targets of influence

We next sought to identify brain-wide targets of cerebellar influence that could account for the observed perseverative and inflexible behavior. To quantify expression of the activity-dependent immediate early gene c-Fos, we extracted brains at different points in the Y-maze learning and reversal paradigm (Dragunow and Faull, 1989). We compared the effects of lobule VI and crus I perturbations with closely-matched control conditions (see **Methods, Whole-Brain Imaging** for description). Brains were cleared using iDISCO+ (Renier et al., 2014) and immunostained for c-Fos and the mCherry fluorescent tag encoded by both DREADD and control AAVs (**movie supplement 3**). Samples were imaged for AlexaFluor-647 on a light-sheet microscope, aligned to the Princeton Mouse Atlas (De Zeeuw, 2021; De Zeeuw et al., 2021; Leiner et al., 1993, 1986; Pisano et al., 2022, 2021), and analyzed for c-Fos positive cells using ClearMap (Renier et al., 2016) (**Figure 4A; movie supplement 3**). Using 122 chosen structures, a 3-D representation of the data was created for each brain using Neuroglancer, a Google WebGL-based viewer for volumetric data (**Figure 4A**) for analysis of c-Fos in single or combined regions (**Figure 4B**).

Within each paired comparison, we processed brains from all control and treatment animals as a single batch using the same tissue preparation and imaging conditions whenever possible. In the few cases where we needed multiple batches, we adjusted for confounding batch effects by including indicator variables as covariates in regression models. Analogous to genome-wide association studies, we analyzed each brain region independently and corrected the results

post hoc for false discovery rate. For each region, we quantified the contrast between counts for the animals in the treatment group versus the control group using negative binomial regression with a log link function. To account for animal-specific variation in total count, we included the log of total counts as an offset (**Figure 4C**).

To identify brain regions activated in the initial acquisition of Y-maze learning, we assayed c-Fos-positive cells immediately after 3 days of Y-maze ending on the last initial acquisition day (n=10 mice), using for baseline comparison animals that underwent habituation-only on the first day of Y-maze (n=10 mice). Out of 122 regions, 33 regions showed increased activity and 6 regions showed decreased activity. We found activation in thalamus (1.4-fold) and in prelimbic (1.8-fold) and temporal association (1.65-fold) cortex. In the rest of the brain, we found some of the strongest associations in parabrachial nucleus (2.8-fold), basolateral, central, and cortical amygdalar nucleus (1.8, 1.7, and 1.7-fold), lateral habenula (2.3-fold), periaqueductal gray (2.1-fold), septohippocampal nucleus (2.9-fold), and lateral septal nucleus (2.6-fold) (**Figure 5-figure supplement 1** and **Figure 6-figure supplement 1C, Figure 6-figure supplement 2**). We confirmed results in the parabrachial nucleus using conventional immunohistochemistry ($p = 0.00006$, Cohen's $d = 1.4$) (**Figure 6-figure supplement 1A-B)**. Overall, initial learning specifically activated a wide range of regions linked with associative and affective function.

Wwe analyzed specific neural correlates of reversal learning by comparing brains on day 4 after one day of reversal learning (n=10 mice) with mice undergoing a third day of acquisition (n=8). We found statistically significant activation throughout thalamus (2.7-fold), including polymodal regions (3.2-fold) as classified by Jones, sensory/motor regions (2.1-fold), and the reticular nucleus, which is modulatory (3.2-fold) (Burton and Jones, 1976; Jones, 2012). Reversal learning was associated with decreases in the majority of neocortical regions, the largest change being a decrease in infralimbic cortex activity (0.56-fold). Additional activation occurred in medial and lateral habenula (15.6-fold and 7.6-fold), periaqueductal gray (1.9-fold), and parabrachial

nucleus (1.6-fold) (**Figure 4, Figure 4-figure supplement 1, Figure 6A, Figure 6-figure supplement 2**).

We tested the effects of lobule VI perturbation (n=10 mice) on c-Fos generation in reversal learning. Perturbation of lobule VI during reversal learning resulted in a reduction in c-Fos activity throughout the thalamus (overall 0.28-fold compared with unperturbed reversal learning). Increased activity was seen in somatomotor, somatosensory, anterior cingulate, and infralimbic cortex. Midbrain regions both increased (ventral tegmental area, lateral hypothalamus, midbrain raphe nuclei) and decreased (parastrial, medial and lateral habenula, and periaqueductal gray) in activity (**Figure 5 A-C, Figure 6A and C, Figure 6-figure supplement 1D-F, Figure 6-figure supplement 2**). Thalamic results were confirmed using conventional immunohistochemistry ($p = 0.000002$, Cohen's $d = 2.3$) (**Figure 6-figure supplement 1D-E)**. Such widespread changes were not seen when giving CNO during an additional day of acquisition (**Figure 5D)**.

We also examined the consequences of bilateral crus I perturbation on reversal learning. Bilateral perturbation of crus I during reversal learning did not lead to statistically detectable changes in thalamic activity compared with unperturbed reversal learning. However, changes were seen in the neocortex, both increases (anterior cingulate, prelimbic, infralimbic, and orbital) and decreases (auditory, visual, posterior parietal, and temporal). Increases were also seen in parastrial nucleus and hypothalamus (lateral and preoptic) (**Figure 6A-B**). These changes were not seen after unilateral perturbation of crus I (**Figure 5-figure supplement 1**).

Many effects of lobule VI and crus I perturbation went in the opposite direction as the reversal-versus-acquisition condition. Of the 61 regions showing changed activity in reversal learning, opposite-direction changes occurred in 47 regions from lobule VI perturbation, and in 27 regions from crus I bilateral perturbation. Opposite-direction changes encompassed the majority of thalamic regions and lateral and medial habenula, as well as selected regions in telencephalon (anterior cingulate, infralimbic) and mesencephalon (periaqueductal gray, pretectal regions) with a lobule VI perturbation (**Figure 6A)**. The overall pattern of cell ratios was strongly correlated with

the reversal-versus-acquisition condition for lobule VI (correlation of log-cell-ratios by Pearson's r = -0.78) (**Figure 6C)**, and less correlated for bilateral crus I (Pearson's r =-0.29) **(Figure 6B)**. Thus, lobule VI perturbation reversed activation patterns in most regions that were activated by reversal learning, while crus I perturbation had effects that were limited to neocortical and hypothalamic regions.

Discussion

We found that intact cerebellar function in lobule VI and crus I was necessary for two acquired flexible behaviors, adaptation to an open field, and choice reversal in a swimming Y-maze. In both behavioral paradigms, silencing of Purkinje cells led to deficits that became apparent over a period of several days, and in the case of Y-maze was marked by incorrect repetitive choices even in a forced session. Y-maze choice reversal recruited activity in a diencephalon-centered group of regions, most of which were reversed by inhibition of Purkinje cells in lobule VI; and in prefrontal and hypothalamic regions, which were reversed by inhibition of either lobule VI or crus I. Taken together, these studies comprise a demonstration of cerebellar perturbation leading to specific alterations in whole-brain activity and nonmotor function.

Identification of effects on flexible behavior required us to distinguish them from changes in the coordination of movement. Our pose analysis (Klibaite et al., 2022) enabled us to simultaneously analyze the detailed kinematics of limb movement and longer time-scale features of behavior. Such an analysis required a method that could track individual body parts, such as LEAP (Pereira et al., 2022, 2019) or other approaches (Wiltschko et al., 2020, 2015); (Mathis et al., 2018; Nath et al., 2019). We did not find differences in gait or in spatial occupancy of the arena, suggesting that the chosen cerebellar perturbations affected the evolution of motor behaviors over several days, but not the capacity to interact with the physical environment or generate locomotor behavior. These results are consistent with past work in which rodent gait was not altered by lobule-specific perturbation of posterior cerebellum (Badura et al., 2018;

Stoodley et al., 2017), but was changed by cerebellum-wide disruption (Klibaite et al., 2022; Machado et al., 2015; Tsai et al., 2012).

Flexible cognition, as examined by Y-maze reversal learning, was found to be strongly modulated by lobule VI and crus I. Mice demonstrated perseveration in this task by swimming repeatedly toward the previously learned arm before finding the platform in the third arm of the Y-maze, even when the incorrect arm was blocked. Perseverative behavior is a principal criterion for autism spectrum disorder (Maes et al., 2011; Reese et al., 2003; Sasson et al., 2008). Vermal lobules VI-VII are altered in their volume developmental trajectory in ASD children compared with the rest of cerebellum (Crucitti et al., 2020; Traut et al., 2018), suggesting a specific role for lobule VI in driving ASD-like outcomes. In the open field, lobule VI-perturbed mice demonstrated reduced adaptation by staying in a fast locomotive state on both days. Given the widespread disruption of thalamic activity caused by inhibiting lobule VI output, these behavioral deficits may arise from the disruption of sensory or polymodal processing, reducing the capacity of the forebrain to detect novelty or process its consequences.

We found that disruption of crus I altered both multiday adaptation to the open field and the ability to reverse learning in a swimming Y-maze. Crus I has been implicated in social processing both in mice and in humans with ASD (Kelly et al., 2020; Stoodley et al., 2017) and crus I is engaged in the processing of sensory novelty in human studies (Caulfield et al., 2016; Ottaviani et al., 2016). Due to the spread of injections, crus II may be an additional route by which our experiments affected behavior. Taken together, our findings are in accordance with lobule-specific substrates for a number of deficits that arise in cerebellar cognitive-affective disorder (Schmahmann, 2013, 2004; Schmahmann and Sherman, 1998).

The cerebellum influences the rest of the brain through polysynaptic paths through the deep and vestibular nuclei. By analyzing the immediate-early gene c-Fos, we found that reversal learning engaged midbrain, diencephalic, and neocortical regions associated with flexible behavior, and that this engagement was reversed by perturbation of lobule VI. Many of these

brain regions receive disynaptic paths from lobule VI and crus I, as demonstrated by transsynaptic tracing (De Zeeuw, 2021; De Zeeuw et al., 2021; Leiner et al., 1993, 1986; Pisano et al., 2021). In the midbrain, the habenula, periaqueductal gray, and parabrachial nucleus are engaged during defensive, negative-reward, and decision-making behavior (Andres et al., 1999; Chiang et al., 2019; Deng et al., 2016; Hu et al., 2020). Finally, the infralimbic and anterior cingulate cortex are activated in effective decision making and reward-seeking (Boulougouris et al., 2007; Capuzzo and Floresco, 2020; Ghahremani et al., 2010). Our observation that lobule VI and crus I inhibition affects activity in these regions during reversal learning suggests that cerebellar activity is necessary for the normal expression of a wide range of brain activity in the face of changing environmental valence.

Recent studies show that vermal and hemispheric regions project via the deep cerebellar nuclei to distinctive patterns of forebrain structures (Chao et al., 2022; De Zeeuw, 2021; De Zeeuw et al., 2021; Fujita et al., 2020; Leiner et al., 1993, 1986), influencing thalamocortical nonmotor processing. Chemogenetic inhibition of lobule VI Purkinje cells led to broad decreases in thalamic activity as measured using c-Fos. We note that other early-immediate genes may also be activated during these tasks and can be analyzed in future experiments. A major target of cerebellar output, especially from lobule VI/VII, is the thalamic reticular nucleus (De Zeeuw, 2021; De Zeeuw et al., 2021; Leiner et al., 1993, 1986; Pisano et al., 2021), which is inhibitory and sends its outputs throughout the rest of the thalamus. Reticular nucleus paths have been suggested to have a gating effect on thalamocortical function (Halassa and Kastner, 2017) and are important for flexible behavior (Cavdar et al., 2002; Guillery and Harting, 2003; Harting et al., 1991; Houser et al., 1980). In addition, removal of Purkinje-cell inhibition in lobule VI might be expected to increase activity in thalamic polymodal nuclei via cerebellothalamic excitation, providing a means by which effects might differ across thalamic nuclei. The fastigial nucleus, which receives strong lobule VI input, has recently been shown to send output to brainstem targets subserving arousal and autonomic functions (Fujita et al., 2020)(De Zeeuw, 2021; De Zeeuw et

al., 2021; Leiner et al., 1993, 1986). The widespread nature of lobule VI's functional targets supports the idea that the cerebellum acts as a powerful modulator of thalamocortical processing in situations that call for flexible behavior.

Chemogenetic inhibition of crus I Purkinje cells also led to changes in neocortical activity as measured using c-Fos. Crus I (De Zeeuw, 2021; De Zeeuw et al., 2021; Leiner et al., 1993, 1986; Pisano et al., 2021) projects to thalamus, both sensory/motor such as ventral posteromedial nucleus and polymodal such as lateral dorsal nucleus, and to hypothalamus, which like the thalamus is a diencephalic structure that projects monosynaptically to neocortex (Saper, 2000). Transsynaptic paths from crus I project particularly densely to infralimbic, prelimbic, and orbital cortex, providing a substrate for our observed alterations in c-Fos expression.

Lobule VI perturbation changed thalamic c-Fos activation more than it changed neocortex, and crus I perturbation changed neocortex but not thalamus. One obvious explanation is that neocortex receives inputs from many nonthalamic sources, and indeed disjoint activation of thalamus and neocortex has been long known (Fuller et al., 2011; Vanderwolf and Stewart, 1988). Mapping of c-Fos may also fail to capture all relevant changes. Expression of c-Fos depends in a complex and cell-type-dependent manner on activity (Fields et al., 1997). Furthermore, c-Fos expression persists for many minutes, far longer than the timescale of synaptic chains of activation (<1 s). Thus, our results could have potentially arisen from later events including long-term consequences of failing to complete the task.

Lateralization of cerebellar function has previously been reported both in mice and in humans with ASD (Kelly et al., 2020; Stoodley et al., 2017). We observed some lateralization of effect for right crus I perturbation on open-field adaptation, but not Y-maze reversal. Left-right lateralization might be expected to be opposite to that of neocortex because ascending paths decussate on the way from deep nuclei to thalamus. However, when the ascending connection from cerebellar cortex is traced, ipsilateral and contralateral paths to nonmotor cortex are similar in strength (De Zeeuw, 2021; De Zeeuw et al., 2021; Leiner et al., 1993, 1986; Pisano et al.,

2021), suggesting that any cerebellar lateralized function should either be weaker or differ from neocortex.

In summary, we have used chemogenetic inhibition of Purkinje cells to identify two cerebellar regions that influence multiday flexible behavior, lobule VI and crus I. Detailed characterization of c-Fos activation in Y-maze, including different stages of learning (habituation, acquisition/“nonreversal”, and reversal), revealed brainwide consequences of the task and focal perturbations. First, more challenging task conditions led to progressively more widespread regional activation. Second, cerebellar perturbation affected activity in regions that were activated under reversal learning, including thalamus by lobule VI and neocortex by crus I. Brain-wide c-Fos mapping serves as a screen analogous to the introduction of the Genome-Wide Association Study in 2002 (Ozaki et al., 2002). Understanding the task-specific role for cerebellum in driving forebrain neural processing will require direct recording or high-time-resolution perturbation of the candidate regions we have identified.

Methods

Key Resources Table

Reagent type (species) or resource	Designation	Source or reference	Identifiers
gene		NA	
strain, strain background	Mouse :C57BL/6J	The Jackson Laboratory, Bar Harbor, ME	Stock#: 00664 |Black6 https://www.jax.org/strain/000664
strain, strain background	Mouse: *Pcp2*^{Cr}	The Jackson Laboratory, Bar Harbor, ME	Stock#: 004146 https://www.jax.org/strain/004146
genetic reagent		NA	
cell line		NA	
transfected construct		NA	
biological sample		NA	
antibody	anti-GFP chicken	Aves Labs	Cat#GFP-1020; RRID: AB_10000240

antibody	goat anti-chicken IgY (H+L) secondary antibody, Alexa Fluor 647	ThermoFisher	Cat#A-21449; RRID: AB_2535866
recombinant DNA reagent	AAV1-Eflα-DIO-hM4D(Gi)-mCherry-WPRE-hGHpA;AAV8-Eflα-DIO-mCherry-WPRE-hGHpA	Princeton Vector Core	
recombinant DNA reagent	AAV1-sL7-Cre-HA-WPRE-hGH-pA	Princeton Vector Core	
recombinant DNA reagent			
sequence-based reagent		NA	
peptide, recombinant protein		NA	
commercial assay or kit		NA	
chemical compound, drug	Clozapine-N-oxide (CNO)	NIMH Chemical Synthesis and Drug Supply Program	Cat# 34233-69-7
chemical compound	ProLong™ Diamond Antifade Mountant	ThermoFisher	Cat# P36961
chemical compound, drug	15% D-mannitol	SIGMA-ALDRICH	Cat# M4125
chemical compound	DPBS	ThermoFisher	Cat#14190136
chemical compound, drug	white tempera paint	Artmind, Tempera Paint	Cat#10091773
chemical compound, drug	Rimadyl [carprofen]	Zoetis, Florham Park, NJ	http://www.zoetisus.com
chemical compound	cholera toxin subunit B (CT-B), AlexaFluor 488 Conjugate	ThermoFisher	Cat# C34775
chemical compound, drug	ketamine/xylazine	Met-Vet International/Akorn	RXV CIII (3N)/Cat# 59399-111-50
chemical compound, drug	Euthasol	Met-Vet International/Virbac	RXV CIII (3N)/ RXEUTHASOL
chemical compound,	CM-DiI	Thermofisher	Cat # C7000

software, algorithm	Illustrator CS	Adobe	
	Excel	Microsoft	
	MATLAB R2020b	MathWorks	
	Python 2.7.14/3.8.6	Python	
	R 4.0.3	R	
	ImageJ	NIH	
	Neuroglancer	(Google WebGL-based viewer)	
	Allen Brain Atlas	(Oh et al., 2014).	http://www.brain-map.org
Resource Availability	Data for this manuscript	Princeton database	https://doi.org/10.34770/c9df-sc15
	Data from Klibaite et al., 2022	Princeton database	https://dataspace.princeton.edu/handle/88435/dsp012j62s793m
	Code	Github	https://github.com/PrincetonUniversity/OF-ymaze-cfos-analysis

Experimental Design

To investigate the role of cerebellar lobule-specific roles in a flexible cognitive task, we targeted neural activity of Purkinje cells of mice using Designer Receptors Exclusively Activated by Designer Drugs (DREADDs). We delivered adeno-associated virus (AAV) with the sequence for the inhibitory DREADD hM4Di, which was fused to mCherry protein under a Ef1α promoter. This virus included a DIO component, which when combined with the L7-cre virus, expressed in the Purkinje cell layer exclusively (**Figure 1A; Figure supplement 1A-C**). Mice used in this study were male C57BL/6J (The Jackson Laboratory, Bar Harbor, ME) and acclimated for at least 48 hours at the Princeton Neuroscience Institute vivarium prior to procedures. After a three-week recovery period, mice (PND 70) underwent behavioral testing starting with social behavior, then open field, and water Y-maze reversal for whole-brain c-Fos analysis (**Figure 1I**). Recently clozapine-N-oxide (CNO) has been found to convert back to the parent compound, Clozapine, in mice prior to crossing the blood-brain barrier. To reduce confounds in our experimental design, all mice received CNO during all behavioral tasks, as Clozapine may alter signaling of

neuromodulators, notably dopamine and serotonin (Gomez et al., 2017; Jendryka et al., 2019; Manvich et al., 2018).

For DREADD electrophysiology and behavioral experiments, lobules targeted were lobule VI (n = 36 behavior, n = 10 for recordings), bilateral crus I (n = 17), crus I right (n = 25), crus I left (n = 26), but as AAV can spread into neighboring lobules, mCherry fluorescence was recovered and quantified for the entire cerebellum. Controls included animals injected with AAV without DREADDs (CNO and mCherry, n = 18), CNO only (n = 30), Vehicle (DMSO and saline, n = 9), and untreated (n = 123). To understand if CNO or a lobule-specific perturbation altered Y-maze performance without reversal a subset of CNO only (n = 7) and CNO and Lobule VI mice (n = 10) underwent 25 trials of a third day of acquisition. To understand learning in the Y-maze, animals were sacrificed after habituation (n = 16), acquisition day 1 (n = 16), and acquisition day 2 (n = 10) for a total of 42 mice. When conditions allowed, the same animals went through both water Y-maze and open field testing, see **Table 1**. All mice were housed in Optimice cages (Animal Care Systems, Centennial, CO) and received environmental enrichment, including paper nesting strips and one heat-dried virgin pulp cardboard hut (Shepherd Speciality Papers, Milford, NJ). Mice were fed PicoLab Rodent Diet food pellets (LabDiet, St. Louis, MO) and water was provided ad libitum. Cages were changed every two weeks and animals were housed in groups of 4-5 mice in reverse light cycle rooms to maximize normal nocturnal activity, as behavior testing occurred during the day. All experimental procedures were approved by the Princeton University Institutional Animal Care and Use Committee and in accordance with animal welfare guidelines of the National Institutes of Health.

Animal preparation

Mice underwent surgery similar to previous published procedures (Badura et al., 2018; Giovannucci et al., 2017; Kloth et al., 2015) at postnatal day 56. Briefly, animals were

anesthetized with isofluorane (5% induction, 1-2% oxygen; 1 L/min) and mounted in a stereotaxic device (David Kopf Instrument, Tujunga, CA) for all surgeries. Temperature was monitored and automatically adjusted using PhysioSuite (Kent Scientific Corporation, Torrington, CT). Animals were prepared for surgery with an application or Puralube vet ointment (Pharmaderm Florham Park, NJ) to prevent corneal drying, the scalp was shaved and cleaned, and animals received osmotic diuretic drug 15% D-mannitol in DPBS (0.02ml/g; intraperitoneal, i.p.) and an anti-inflammatory drug, Rimadyl (5mg/kg Carprofen 50 mg/ml, Pfizer, Eurovet, in NaCL; every 24 hours for 2 days; subcutaneous, s.c.). A lateral skin incision was made over the lambdoid suture. Muscle was cut over the occipital bones first vertically than horizontally and as close to the bone as possible to allow for regrowth post-surgery and enough to expose lobule VI or crus I. A small craniotomy was made over each lobule of interest for injection of inhibitory DREADD AAV1-Eflα-DIO-hM4D(Gi)-mCherry-WPRE-hGHpA (8.5 x 10^13; PNI Vector Core, AAV-VC68) or control AAV8-Eflα-DIO-mCherry-WPRE-hGHpA (1 x 10^15; PNI Vector Core, AAV-VC139). To target Purkinje cells, both DREADD and control AAVs were mixed in a 1:1 ratio with AAV1-sL7-Cre-HA-WPRE-hGH-pA (2 x 10^14; PNI Vector Core, AAV-VC141). Confirmation of mCherry expression and Purkinje cell inhibition by DREADD activated by CNO was determined (**Figure 1C-D**). Virus was injected using borosilicate glass capillaries (World Precision Instrument, Sarasota FL) made using the Sutter Micropipette Puller (Model P-2000, Sutter Instrument Company) and bevelled at a 45 degree angle. To ensure viral spread ~600nl total of DREADD or control was injected per mouse, distributed at 3 separate depths (150, 250, 450 µm below the dura) and two locations per lobule. Craniotomy was sealed with a silicone elastomer adhesive (Kwik-Sil, World Precision Instrument, Sarasota, Fl) and skin was sutured. All mice were tested two weeks post-surgery at P70.

Tissue processing and histology

To examine mCherry fluorescence, the presence of DREADD virus, two mice were anesthetized with Euthasol (0.06 ml/30g, i.p.) and perfused with 4% paraformaldehyde (PFA). Brains were stored overnight at 4% PFA then placed in 20% sucrose in PBS overnight until sectioning at 50 µm. Sections were washed with PBS and incubated for 1 hr at room temperature (RT) in blocking buffer (10% normal donkey serum, 0.5% Triton in PBS) prior to an overnight incubation at 4℃ in PBS buffer with 2% normal donkey serum, 0.4% Triton and the rabbit anti-RFP (600-401-379, Rockland Immunochemicals, Inc., Limerick, PA; 1:1000) primary antibody. The next day, sections were washed in PBS and incubated for 2 hr at RT in PBS buffer with 2% normal donkey serum, 0.4% Triton, and the donkey anti-Rabbit Alexa Fluor 647-conjugated secondary antibody (A-21449; Thermo Fisher Scientific, MA, USA, Invitrogen; 1:400).Tissue was mounted on glass slides with Prolong Diamond (ThermoFisher Scientific, MA, USA). Tissue was imaged with a Leica SP8 confocal laser-scanning microscope (Leica Microsystems, Germany) using 40x or 63x objectives (**Figure-figure supplement 1B-C**).

To confirm tissue clearing and lightsheet microscopy, brains were sectioned and stained using conventional immunohistochemistry. Free-floating tissue sections were cut using a vibratome (VT-1000S, Leica Microsystems, Germany). After washing in phosphate buffered saline (PBS) ph 7.6 at RT for four 10 min sessions, sections were blocked with 10% donkey serum and 0.5% Triton X-100 in PBS for 1 hr. Post-incubation, sections were placed in the primary solution of rabbit anti-Fos (226 003, Synaptic Systems,Goettingen, Germany, 1:1000) with 2% donkey serum and 0.5% Triton X-100 in PBC for 48 hours at 4°C. Sections were washed for three 10 min sessions in PBS then placed in secondary donkey anti-Rabbit Alexa Fluor 647-conjugated secondary antibody (A-21449; Thermo Fisher Scientific, MA, USA, Invitrogen; 1:200) in 2% donkey serum and 0.4% Triton X-100 in PBS for 2 hr at RT. Sections were washed for three 10

min sessions in PBS. Tissue was imaged at 20x using an epifluorescence microscope (NanoZoomer S60, Hamamatsu Photonics) and c-Fos positive cells were counted in ImageJ (**Figure 6-figure supplement 1A and D**).

After animals completed the last Y-maze reversal session, animals were placed back in their home cage for 90 minutes. Then mice were anesthetized with Euthasol (0.06 ml/30g, i.p.) and perfused with 4% PFA for analysis of c-Fos and mCherry expression for DREADD recovery using iDISCO+ clearing methods (Pisano et al., 2022, 2021; Renier et al., 2014). Briefly, after an overnight fix in 4% PFA, brains were rinsed in PBS at RT for four 30 minute sessions. Immediately brains were dehydrated 1 hr at each ascending concentration of methanol (20, 40, 60, 80, 100, 100%) and placed overnight in 5% hydrogen peroxide and methanol at RT. The next day, brains were rehydrated for 1 hr at each descending concentration of methanol (100, 80, 60, 40, 20%) and lastly PBS. Samples were placed in detergent (0.2% Triton X-100 in PBS) for two 1 hr sessions then placed for two days in 20% Dimethyl sulfoxide (DMSO), 0.3 M glycine, 0.2% Triton X-100 in PBS at 37℃. Brains were blocked in 10% DMSO, 6% donkey serum, 0.2% Triton X-100 in PBS at 37°C for 3 days. Once at RT, samples were washed in PTwh (0.2% Tween-20, 10µg/ml heparin in PBS) and placed in primary solution of rabbit anti-Fos (226 003, Synaptic Systems,Goettingen, Germany, 1:1000) and/or rabbit anti-RFP (600-401-379, Rockland Immunochemicals, Inc., Limerick, PA; 1:450) for one week at 37℃. Brains were washed in PTwH five times in increasing amounts of time (10, 15, 30, 60, 120 min) and then placed in secondary donkey anti-Rabbit Alexa Fluor 647-conjugated secondary antibody (A-21449; Thermo Fisher Scientific, MA, USA, Invitrogen; 1:200) for one week at 37℃. Brains were washed in PTwH five times in increasing amounts of time (10, 15, 30, 60, 120 min) then dehydrated 1 hr at each ascending concentration of methanol (20, 40, 60, 80, 100, 100%) until being placed in 66% DCM/33% methanol for 3 hrs at RT. Brains were cleared with 100% dichloromethane (DCM) for two 15 min steps then placed in 100% benzyl ether (DBE). Brains

were kept in fresh DBE prior to imaging and after for long-term storage. Tissue was imaged using a light-sheet microscope (Ultramicroscope II, LaVision Biotec., Bielefeld, Germany), which will be described in *Methods: Whole-brain imaging*.

Behavioral testing

All behavior testing began at P70 and animals were tested in the following order: (1) open field, (2) water Y-maze. Animals were also tested for three-chamber social preference and novelty seeking (Badura et al., 2018) but showed no effects. For each experiment, animals were allowed to acclimate to the testing room for at least 60 minutes. During this time, animals receiving CNO (1 mg/kg, i.p.) or vehicle (1.5% dimethyl sulfoxide in saline, i.p.) were lightly anesthetized for injection and allowed at least 20 minutes of recovery prior to experiments. Animals performed Y-maze under low white light. For open field mice were recorded under far-red LEDs as it was observed that mice would not enter the middle of the plexiglass arena under white light.

Open Field: Wild-type (n = 60) (Klibaite et al., 2022), mice with a cerebellar perturbation (n = 10 per group) and controls, including CNO only (n = 12), CNO and mCherry (n = 10), and vehicle only (n = 10). Previous data collected (Klibaite et al., 2022) using Purkinje-cell specific tuberous sclerosis 1 gene mutation (L7Cre; $Tsc1^{flox/flox}$) (n = 9) was used as a comparison for gait analysis (**Figure 2-figure supplement 1B).** Animals were placed in an open field arena measuring 45.72 x 45.72 cm (length x width) and 30.48 cm in height with a transparent polycarbonate floor, as previously described (Klibaite et al., 2022). A Point Grey grayscale camera (12-bit grayscale, 1280 x 1024 pixel resolution at 80 Hz) was used to image from below. The soundproof box with ventilation was illuminated with far-red LEDs. To prevent noise disturbance, doors were kept closed during acquisition. Mice received CNO on day 1, if applicable, and vehicle on day 2 to understand how perturbation may alter open field

habituation. Each mouse was recorded for 20 minutes before returning to group housing over two days (first 18 min 46 sec are included in the analysis). Raw images were processed to segment the mouse from the background (median filter) to a final video size of 400 x 400 pixels.

Each frame was aligned for the mouse body axis and body parts were tracked using LEAP (LEAP Estimates Animal Poses) as previously described (Klibaite et al., 2022; Pereira et al., 2019). The LEAP network was trained on 1000 frames to find 18 body parts. Automatic classification of animal behavior was performed using custom MATLAB and Python scripts as previously described (Klibaite et al., 2022). Briefly, distances between 11 body parts (nose, chin, 4 x paw tip, 4 x paw base, where paw connects to leg, and tail base) were calculated and the dimensionality was reduced by projecting on the first 10 PCA components. A wavelet analysis was performed in the lower dimensional space, followed by k-means clustering (k = 100) of the frequency data to obtain behavioral clusters. The 100 behavioral clusters were manually grouped into 6 behaviors (slow explore, grooming, fast explore, reared, turning walk, locomotion) (**Figure 2B**). A majority filter with a sliding window of 11 frames was used on the predicted behaviors for each frame. Centroid metrics were used to calculate distance traveled, and fraction of time in the inner arena. The inner part of the arena was defined as the region of the arena with a distance larger than 150 pixels (approximately 7.6 cm) to all borders of the arena. The borders were obtained using the space explored by the mouse. To calculate the temporal change of the probability to be in fast locomotion within the time of an experiment, a sliding window of size 20001 frames was used. The probabilities at equally distant time points were calculated for each mouse separately, based on which the mean and standard deviation was obtained (**Figure 2C**).

For the shifts in state occupancy, the fractions of time spent in each behavior during the first five minutes and the remainder of the experiment were calculated for each mouse. Then, the geometric mean was taken for each group and day and the geometric mean values for day

2 were divided by the ones from day 1 for each group (**Figure 2D; Figure 2-figure supplement 2D**). The shifts in state transitions were obtained as follows: First, the transition matrices were calculated for each mouse and day by considering only changes of states as transitions (i.e. the transition rate to stay in the same state is zero). Then, the transition matrices are averaged for each group and day by weighting the transition probabilities from initial state i by the probability of the mouse to be in state i. Finally, the resulting averaged transition matrix for day 1 is subtracted from the one for day 2 for each group, which allows an investigation of the changes in state transitions across days (**Figure 2-figure supplement 1E**). To study the possibility of gait changes in cerebellar perturbed mice compared to controls, the phases when the paws enter stance during a single stride of locomotion were calculated for different centroid velocities (Machado et al., 2015). The beginning of the stance phase was determined by the peak position of the paw in an animal-centered coordinate system (**Figure 2-figure supplement 1B**). All analyses of the open field behavioral data were performed using custom Matlab code (https://github.com/PrincetonUniversity/OF-ymaze-cfos-analysis).

Water Y-maze: The water Y-maze assay and analysis was similar to described (Badura et al., 2018). Briefly, the Y-shaped transparent polycarbonate apparatus had symmetrical arms, each measuring 33 cm x 7.5 cm x 20.3 cm (length x width x height) from the center. Notches in all three arms (9.5 cm from the center) allowed for a removable gate. A Pyrex glass container was used as a platform for the mice to climb on. To prevent the animals from seeing the platform, opaque water was used by mixing ACMI certified hypoallergenic non-toxic white paint (Art-Minds, Tempera Paint) in warm water. Water levels were kept at a depth to prevent the animals from touching the bottom of the maze. Between each mouse, excrement was removed and water was exchanged to maintain ideal water temperature between 22-28 degrees Celsius. At the end of the day, water was removed for cleaning by PREempt disinfectant wipes (0.5% Hydrogen Peroxide) and sprayed down with 70% ethanol to be left overnight to dry. To prevent distraction, a three-walled shield was placed around the maze constructed of non-reflective

black plastic (34 x 29 x 22 cm, length x width x height). Directly above the arena, a camera (PlayStation Eye) was mounted on a T-slotted aluminum rail (80/20 KNOTTS Company, Berkeley Heights, NJ) and used to record the entire field of view at 50 frames/s using a custom Python 2.7.6 script (Anaconda 1.8.0) and a CLEye Driver (https://codelaboratories.com/products/eye/driver/).

Over four consecutive days animals were habituated to the arena (Day 1; three 60 s trials), learned to find a platform through trial and error (Acquisition Day 2 and Day 3; four sessions with five 40 s trials), then exposed to reversal whereby the platform was moved to the opposite arm the animals learned (Day 4; five sessions with five 40 s trials) (**Figure 3A)**. Mice were required to have 80% success rate for acquisition day 3 in order to progress to the reversal day. During the reversal day, animals were exposed to four sessions of five consecutive trials followed by a fifth forced session whereby a door was placed in the initial learned arm of the maze which no longer has a platform. All mice were kept in a clean cage on a heating pad to dry before returning to their homecage. As the temperature difference between the warming cage and the water can be drastic, it is critical to allow for the animal to cool down prior to starting a new session. Performance on first-choice turn direction in the Y-maze assay was calculated automatically. Neither surgery by itself, nor the effects of administering vehicle-only, CNO-without-DREADD, or CNO-with-mCherry, affected distance swum, initial learning, or reversal-learning compared with untreated mice (**Figure 3-figure supplement 1A-C**). Distance traveled during habituation was calculated to assess possible muscle damage during surgery (**Figure 3-figure supplement 1A**). Subsequent tries were recorded to calculate the fraction of choices required to reach the platform (**Figure 3D;Figure 3-figure supplement 1F**).

Whole-Brain Imaging

All brains were analyzed and processed similarly to Pisano et al., 2021 (Pisano et al., 2022, 2021). Briefly, cleared brains were glued (Loctite, 234796) ventral-side-down to a 3D printed holder and imaged in DBE. Brains were registered using the autofluorescence channel (488 nm laser diode excitation and 525 emission) to the Princeton Mouse Atlas. Cellular imaging of c-Fos and mCherry expression was acquired using 640 nm excitation and 680 nm emission (1x magnification, 1.3x objective, 0.1 numerical aperture, 9.0 mm working distance, 12.0 x 12.0 mm field of view, LVMI-Fluor 1.3x, LaVision Biotech) with a 10 μm step-size using a 0.016 excitation NA. Analysis of whole-brain c-Fos was completed using ClearMap (Renier et al., 2016) on high performance computing clusters. To confirm ClearMap cell counts, two human annotators analyzed 14 brain volumes and found 96.72% correspondence between cells counted by the human annotators and ClearMap counted cells. Structures less than 80 microns and structures in the medulla were removed from analysis. The medulla was not analyzed as it can be damaged during brain extraction. Ventricles, brain edge, and zones within 60 microns of region boundaries were removed. The cerebellum was not analyzed for c-Fos activity. Visualization of brain volumes and cell detections from ClearMap was performed using Neuroglancer. Tissue image processing and registration was performed using custom Python code (https://github.com/PrincetonUniversity/BrainPipe).

We assessed the impact of varying experimental conditions in the following contrasts:

1. Acquisition day 1 vs Habituation
2. CNO control reversal vs CNO control no reversal
3. CNO control reversal vs Vehicle control reversal
4. Vector control reversal vs Vehicle control reversal
5. Lobule VI reversal vs CNO control reversal
6. Crus I left vs CNO control reversal
7. Crus I right vs CNO control reversal
8. Bilateral Crus I vs CNO control reversal
9. Lobule VI reversal vs Lobule VI no reversal

In contrasts 1-5, both the control and the treatment groups of mice were processed in the same batch so as to minimize batch effects. In contrasts 6-7, both control and treatment groups were present in multiple batches, so batch (encoded as a categorical indicator variable) was included as a covariate to adjust for the batch effect. Finally, in contrasts 8-9 control and treatment groups did not overlap within any single batch, impeding the direct adjustment for confounding due to batch effects. However, we were able to adjust for confounding indirectly by using a "bridge variable" strategy. A bridge variable is an experimental group found in both the batch containing treatment animals as well as the batch containing control animals. The bridge variables were Lobule VI reversal for contrast 8 and CNO control reversal for contrast 9. Inclusion of the bridge variable along with the batch indicator variables in a regression model makes identification of the treatment versus control contrast statistically identifiable separate from the batch effect.

Each mouse was treated as a single observation or biological replica, consisting of its experimental condition (i.e. treatment or control) and a multivariate outcome of counts of active neurons in each of the brain regions. Total counts of active neurons were highly variable between animals even in the same experimental condition. We therefore sought to explain differences in proportion of total counts for each brain region. Given the overdispersed, discrete nature of the data, we used a negative binomial likelihood and performed separate regressions for each brain region and contrast, using the natural log of total counts as an offset. Specifically, for a given contrast, let X_i=1 if animal i is in the treatment group and X_i=0 otherwise. Let Z_i=1 if animal is in the first batch and Z_i=0 otherwise. Let A_i=1 if the animal has the bridge variable condition and A_i=0 otherwise.Let T_i be the total c-Fos counts across all regions in brain i. Let Y_{ij} be the c-Fos count in region j of brain i. The statistical model is then given by

Y_{ij} ~ negative binomial (μ_{ij},φ_j)

$\log(\mu_{ij}) = \beta_{0j}+X_i*\beta_{1j} + \ln(T_i) + Z_i*\beta_{2j} + A_i*\beta_{3j}$

where μ_{ij} is the expected value of Y_{ij}, φ_j is the nuisance shape parameter of the negative binomial distribution, and β_{0j} is an intercept term which captures the fact that some brain regions have a consistently higher or lower activity level across all animals without regard to their experimental condition (for example this could be because some regions have a larger volume than others).

The parameter β_{1j} is of greatest biological interest. It is interpreted as the average change in proportion of c-Fos activity for region j in the treatment group relative to the control group on the logarithmic scale. For example, if β_{1j}=1.5, the average c-Fos activity for brain region j is estimated to be exp(1.5)=4.48 times higher in the treatment condition compared to the control condition. If β_{1j}= -0.7 (a negative coefficient) average c-Fos activity for brain region j is estimated to be exp(-0.7)=0.5 times lower in the treatment condition compared to the control (ie, the treatment mean is half that of the control mean).

We fit each negative binomial regression using the R package MASS (Venables and Ripley, 2002). In addition to maximum likelihood estimates of the regression coefficients such as β_{1j}, this package also computes a standard error for each coefficient. From these we obtained effect sizes in the form of Wald z-test statistics (estimated coefficient divided by standard error). Under the null hypothesis that there is no change in the average c-Fos expression between the treatment and control groups (i.e. β_{1j}=0), the effect sizes would be expected to follow an asymptotically standard normal distribution. By comparing the computed effect sizes against this null distribution, we obtained p-values. If the p-value was small for a given brain region, it suggested that there was a large difference between the treatment and control groups and the null hypothesis should be rejected for that region. Since a separate statistical test was performed for each brain region, we adjusted raw p-values in each analysis to control the multiple testing false discovery rate (FDR) using the method of Benjamini and Hochberg (Benjamini and Hochberg, 1995).

In rare cases, numerical errors occurred in the MASS package fitting procedure. This is because estimation of the negative binomial parameters (β_{0j}, β_{1j}, β_{2j}, β_{3j}, and φ_j) requires an iterative optimization that can fail to converge. We determined that in most of these cases, the brain region was small and/or irregularly shaped. We therefore dropped such regions from subsequent analysis.

In contrast 8 only, some observations came from batch 201810_adultacutePC_ymaze_cfos, in which brains had cerebellum excised. As a quality control step, we excluded regions with extremely low counts and low variability across all brains in this batch since this would destabilize the regression fitting procedure. Specifically, for each region we counted the number of brains within the batch having a nonzero count value. If the number of nonzero counts was less than two, we excluded the region.

In addition to analyzing individual brain regions, we also fit negative binomial regressions to examine the effects of experimental perturbations on three composite regions consisting of multiple subregions from our original 122: thalamus, sensory/motor, and polymodal association. For each composite region and experimental contrast, we summed the raw c-Fos cell counts of all constituent subregions within each animal. We then fit negative binomial regressions as previously described, with the natural log of the total counts in the entire brain again used as an offset for each animal. This maintained consistency in the interpretation of the regression coefficients and effect sizes by keeping them on the same (proportional) scale as the original analysis. To confirm our c-Fos statistical results, we ran two sample t-tests for each region per condition comparison, and then checked the validity of the resulting p-values using permutation testing. None of the highly significant regions from the negative binomial regression were missing.

Acute brain slice experiments

Mice (C57BL/6J) were prepared as described previously in “Animal preparation” for inhibitory DREADD induction of Purkinje cells at 3-weeks of age (n = 4). Two weeks later, mice were deeply anesthetized with Euthasol (0.06 ml/30g), decapitated, and the brain removed. The isolated whole brains were immersed in ice-cold carbogenated NMDG ACSF solution (92 mM N-methyl D-glucamine, 2.5 mM KCl, 1.25 mM NaH_2PO_4, 30 mM $NaHCO_3$, 20 mM HEPES, 25 mM glucose, 2 mM thiourea, 5 mM Na-ascorbate, 3 mM Na-pyruvate, 0.5 mM $CaCl_2$, 10 mM $MgSO_4$, and 12 mM N-acetyl-L-cysteine, pH adjusted to 7.3–7.4). Parasagittal cerebellar brain slices (270 µm) were cut using a vibratome (VT1200s, Leica Microsystems, Wetzlar, Germany), incubated in NMDG ACSF at 34°C for 15 minutes, and transferred into a holding solution of HEPES ACSF (92 mM NaCl, 2.5 mM KCl, 1.25 mM NaH_2PO_4, 30 mM $NaHCO_3$, 20 mM HEPES, 25 mM glucose, 2 mM thiourea, 5 mM Na-ascorbate, 3 mM Na-pyruvate, 2 mM $CaCl_2$, 2 mM $MgSO_4$ and 12 mM N-acetyl-L-cysteine, bubbled at RT with 95% O_2 and 5% CO_2). During recordings, slices were perfused at a flow rate of 4–5 ml/min with a recording ACSF solution (120 mM NaCl, 3.5 mM KCl, 1.25 mM NaH_2PO_4, 26 mM $NaHCO_3$, 1.3 mM $MgCl_2$, 2 mM $CaCl_2$ and 11 mM D-glucose) and continuously bubbled with 95% O_2 and 5% CO_2.

Whole-cell recordings were performed using a Multiclamp 700B (Molecular Devices, Sunnyvale, CA) using pipettes with a resistance of 3–5 MΩ filled with a potassium-based internal solution (120 mM potassium gluconate, 0.2 mM EGTA, 10 mM HEPES, 5 mM NaCl, 1 mM $MgCl_2$, 2 mM Mg-ATP and 0.3 mM Na-GTP, pH adjusted to 7.2 with KOH). Purkinje neurons expressing mCherry were selected for recordings (**Figure 1C-D**).

In vivo electrophysiological recordings

Two days after performing craniotomy and headplate implantation, animals (n = 6) were habituated to head fixation on the treadmill. The day of the recording, cover was removed from the cranial window and then, a Neuropixels probe 1.0 (Imec, Belgium) (Jun et al., 2017) coated with a fluorescent dye (CM-DiI, Thermofisher) was slowly inserted (0.1 mm per 1 minute) using motorized micromanipulator (MP-225; Sutter Instrument Co.) into the cerebellum with the tip reaching depth of 3-5.5 mm below the brain surface. Once the right depth was reached, the probe was left to rest for 15-30 min, before starting the recording. Sterile saline was used to cover the exposed cerebellum. Signals from 384 electrodes were recorded simultaneously at 30 KHz using the Neuropixels headstage 1.0 and Neuropixels 1.0 PXIe acquisition system (Imec). High-frequencies (>300 Hz) and low-frequencies (<300 Hz) were acquired separately. SpikeGLX software (http://billkarsh.github.io/SpikeGLX/) was used to select the recording electrodes, adjust gain corrections and save data. Tactile sensory stimulation was performed in awake mice using the air puffs (40 ms, 20 psi, randomized inter-trial interval, 100 trials) delivered ipsilateral to the recording site via a small tube (2 mm diameter), approximately placed parallel to the anterior-posterior axis, 10 mm mediolateral and 1 mm anterior to the nose of the mouse, and connected to solenoid valve (The Lee Co.) controlled by paired microcontrollers (Arduino Due) and a single board computer (Raspberry Pi). Timings of air puff stimulation were digitized at 10 kHz with multifunction DAQ module (PXIe-6341 unit with BNC-2110 breakout box, National Instruments) and synchronized with using TTL pulses from PXIe acquisition module. Spikes were sorted offline using Kilosort2 (Steinmetz et al., 2021), using default parameters. Manual curation of clusters were performed using Phy (https://github.com/cortex-lab/phy). After extracting timestamps of each putative single unit activity, peristimulus time histograms and firing rate changes were analyzed and plotted using a custom MATLAB script (**Figure 1E-G; Figure 1-supplement 2**). All recording sites were confirmed by post-hoc

histology, in 100 µm coronal cerebellar sections recording tracks were identified with CM-DiI marks (**Figure 1E**).

Statistics

All statistics were performed using MATLAB, R (rstatix, compositions, npmv, data.table, plyr, ggplot2, ggpubr, car, DescTools), or Python 2 and Python 3 (statsmodels, scipy, matplotlib, numpy). Data are presented as mean ± SD, unless otherwise stated. Group mean comparisons were performed through repeated measures ANOVA (open field) or through one-way ANOVAs with Tukey HSD or Dunnett multiple comparisons post-hoc tests. For each comparison the effect size (Cohen's *d*) or Kolmogorov-Smirnov test was calculated. Normality was tested using the Shapiro-Wilk test, and the homogeneity of variances was tested using Levene's test to determine parametric or nonparametric analysis. If the Shapiro-Wilk test or the Levene's test was significant, the nonparametric Kruskal-Wallis test was performed, followed by pairwise comparisons with Wilcoxon rank sum exact tests (with Benjamini-Hochberg multiple comparison correction). In this case, the Wilcoxon effect size r was calculated for each comparison.

Y-maze performance was measured by the number of successes and failures of each mouse in 5 trials for different sessions and days. To account for the fact that the data were nested and can take only values between 0 and 100% (more specifically 0, 20, 40, 60, 80 and 100%), we fit generalized mixed effect models (GLMM) with a binomial distribution and logit link function to the performance data for acquisition day 2, 3 and reversal day (using glmer function in R package lme4 (Bates et al., 2015). We included the session and the experimental group as fixed effects predictors. Since the performance scores within mice may be correlated, we also incorporated random intercepts in the model. We tested different models (with and without the interaction term of group and session; considering session as a factor or a quantitative variable; with and without random slopes added to random intercepts) and chose the models based on

the Akaike information criterion (AIC) and likelihood ratio tests. The data for acquisition day 2 and day 3 was best described by a model without the interaction term of group and session and random intercepts only. To test for significant differences of the performance of the experimental groups, we performed multiple comparisons of the means (Dunnett contrasts, using the glht function in the R package multcomp) (Hothorn et al., 2008). For the reversal day, we also considered a model that accounts for interactions of group and session and tested for within session differences between the groups (Bonferroni-Holm multiple comparison correction).

The number of structures used for c-Fos analysis were tested for multiple comparisons by calculating the false discovery rate, the coefficient of variation, and by performing permutation tests on each comparison. All c-Fos data is presented as $p<0.01$ unless otherwise stated. To analyze correlations between whole-brain c-Fos/DREADD and behavior, Spearman's rank correlation coefficient (ρ) and p-values were determined using stats models in Python 3.

To investigate differences between the behaviors of mice in the open field we performed a compositional data analysis to account for the compositional nature of the data (Martín Fernández et al., 2015). First, for each mouse, the set of fractions of time spent in each behavior were transformed into isometric log ratio coordinates using the R package ‘compositions’. In this coordinate space, differences between groups were analyzed using a nonparametric multivariate test (Wilks’ Lambda type test statistics) from the R package ‘npmv’. To identify the behaviors that differ between groups, we calculated the bootstrapped 95% confidence intervals (N=5000) of the log ratio differences between the cerebellar perturbed groups and mice without a cerebellar perturbation given CNO on day 1 for each behavior (Martín Fernández et al., 2015). The same compositional data analysis was performed on the different control groups using the geometric mean values of all control groups combined as a reference group. The Matlab and R code used for the statistical analyses is published on Github (https://github.com/PrincetonUniversity/OF-ymaze-cfos-analysis).

Acknowledgements:

We thank Henk-Jan Boele, Ben Deverett, Esteban Engel, Laura Lynch, Christina Matl, Dafina Pacuku, Tiffany Pham, Sanjeev Janarthanan, and Fred Uquillas for collaboration and discussion, Greg Horwitz for the L7 plasmid, and Archit Verma and Barbara Engelhardt for discussions on statistical testing. This work was supported by NIH R01 RS045193 and R01 MH115750 (S.W.) and the New Jersey Brain Injury Research Council (J.V.).

Author Contributions:

Jessica L Verpeut: Conceptualization, data analysis and curation, funding acquisition, validation, investigation, visualization, methodology, writing, and project administration.

Silke Bergeler: Data analysis and curation, investigation, visualization, writing.

Mikhail Kislin: Validation of CNO effects on DREADD-expressing Purkinje cells and resulting changes to deep cerebellar nuclei. Data analysis and curation.

Austin Hoag: Data curation, analysis and visualization of c-Fos data.

Thomas J. Pisano: Design and methodology development of whole-brain c-Fos experiments, data acquisition and analysis for c-Fos and injection site recovery.

F. William Townes: Statistical analysis of c-Fos data.

Ugne Klibaite: Data analysis software, curation, investigation.

Junuk Lee: Validation of CNO effects on DREADD-expressing Purkinje cells.

Caroline Jung: Surgical procedures and behavioral testing.

Kelly M. Seagraves: Data analysis and curation.

Joshua W. Shaevitz: Conceptualization, data analysis, funding acquisition, methodology, and project administration.

Samuel S.-H. Wang: Conceptualization, data analysis, funding acquisition, visualization, methodology, writing, and project administration.

Competing interests

The authors declare that they have no competing interests.

Data Availability

The dataset is available at Princeton data DOI: https://doi.org/10.34770/c9df-sc15 and https://brainmaps.princeton.edu/2022/01/verpeut-et-al-data-exploration-links/

Code availability

All experimental and analysis code is available here: https://github.com/PrincetonUniversity/OF-ymaze-cfos-analysis

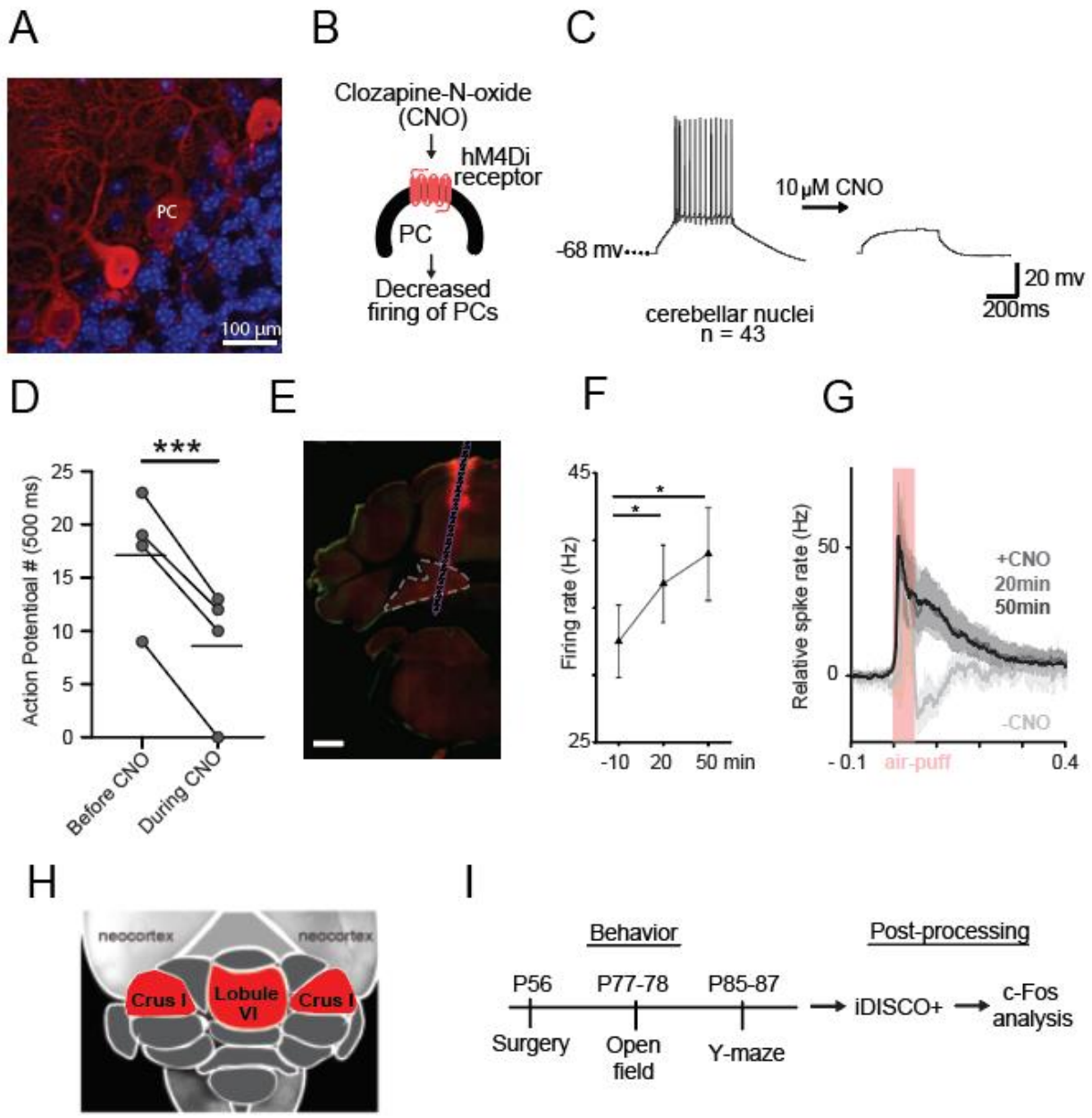

Figure 1. Acute adult inactivation of Purkinje cells in the cerebellar cortex. (A) Expression of the chemogenetic DREADD probe in Purkinje cells (red). (B) The activating ligand clozapine-N-oxide (CNO) binds to the hM4Di receptor and decreases firing of Purkinje cells. (C) Slice electrophysiology of Purkinje cells before and during CNO (10 µM). (D) Purkinje cells with DREADD receptors fire fewer action potentials in response to current injection. (E) Example histological section with the probe location marked by CM-DiI (red), scale bar, 0.5 mm. (F) Average spontaneous firing rate of deep cerebellar nuclei neurons increases after activation of DREADD receptors in Purkinje cells. (G) Average response (averaged across all sensory stimulation and all sorted units, background subtracted and normalized) in deep cerebellar

nuclei (mean ± confidence interval) before and 20, 50 min after CNO injection (n = 5 mice). (H) Dorsal view of the cerebellum with targeted lobule VI or crus I indicated in red. (I) Adult mice received surgery for viral AAV injection (DREADDs or mCherry) at P56 for behavioral testing starting with open field between P77-78 and water Y-maze starting between P85-87. For each behavior test, animals received CNO (i.p.), vehicle, or no treatment 20 minutes prior to testing. After behavioral testing, brains were cleared for light-sheet microscopy using iDISCO+ and analysis of c-Fos immunopositive cells. Comparisons were made using a paired t-test. * $p<0.05$, *** $p < 0.001$

Group	DREADDs	CNO	Open Field	Y-maze
Untreated*	no	no	60	63
Vehicle only	no	no	9	9
CNO only	no	yes	12	22, 7: no reversal
mCherry	no	yes	10	18
Lobule VI	yes	yes	10	16, 10: no reversal
Crus I bilateral	yes	yes	10	7
Crus I right	yes	yes	10	25
Crus I left	yes	yes	10	26
L7Cre; Tsc1$^{flox/flox*}$	no	no	9	0

Table 1: Experimental groups denoting DREADD and CNO conditions. Animals underwent surgery for an injection of DREADD or mCherry viral expression. Prior to open field and the water Y-maze task, animals were injected with the DREADD ligand (CNO), Vehicle, or remained untreated. * Denotes previous data from (Klibaite et al., 2022).

Centroid tracking

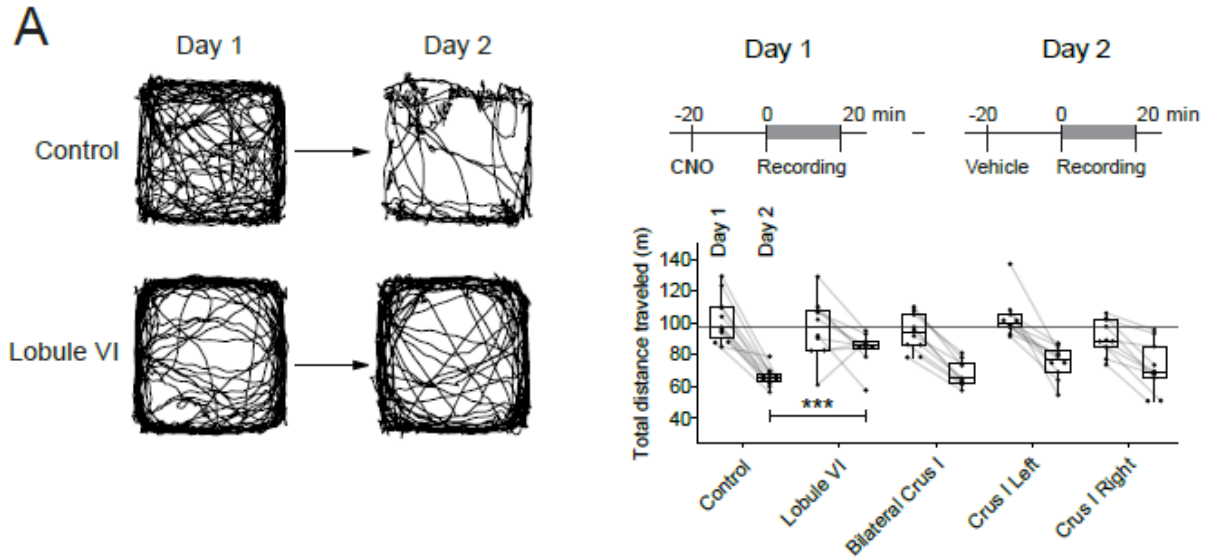

Body part tracking and behavioral classification

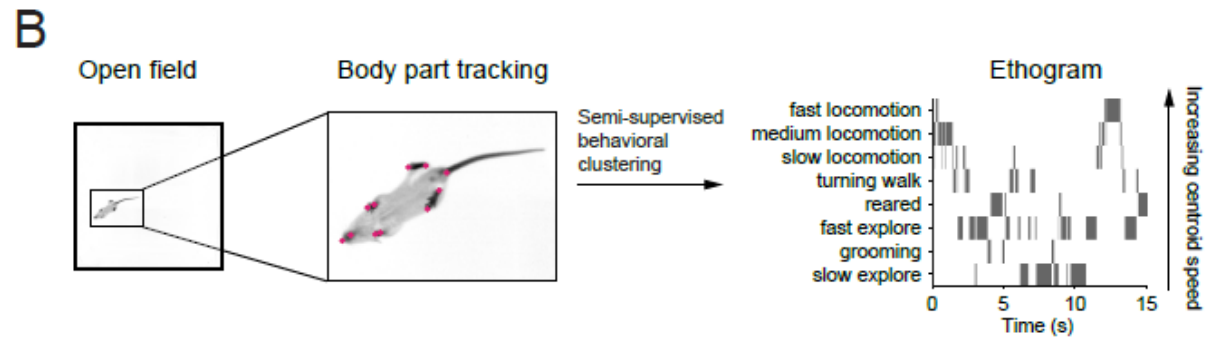

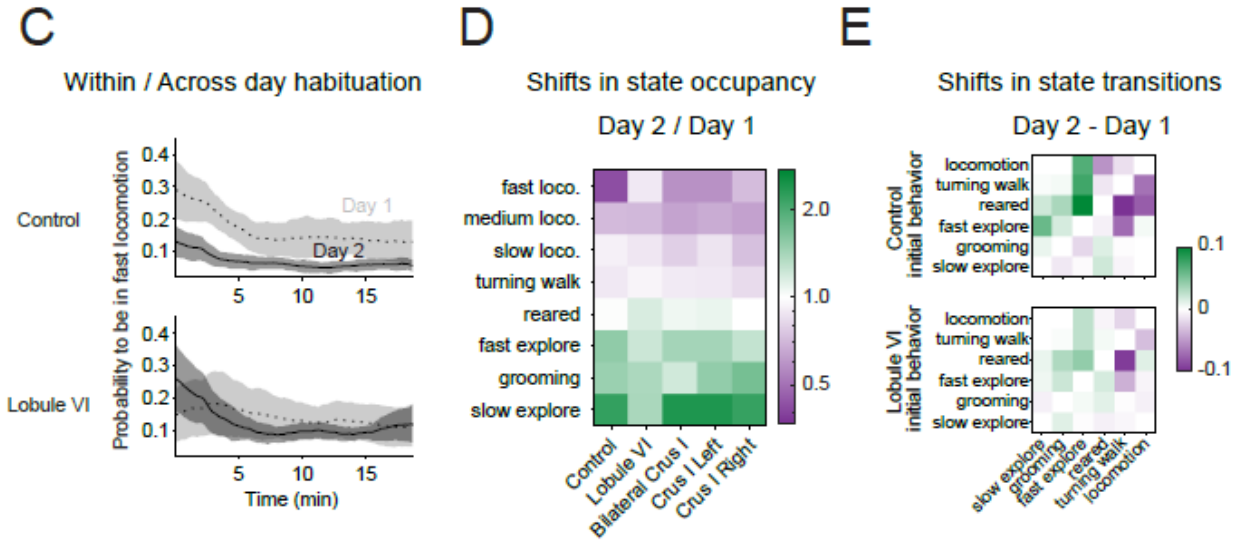

Figure 2. Effects on spontaneous behavior after perturbation of lobule VI and crus I. (A) Lobule VI-perturbed mice show a larger total distance traveled on the second day compared to a day-matched CNO only control group. Left: Example trajectories of the centroid position of a lobule VI-perturbed mouse and a control mouse in the open field for the first 5 minutes. Top right: Timeline of the open-field experiments. Comparisons were made using an one-way or two-way mixed ANOVA. (B) Machine learning pipeline to obtain ethograms for the open-field recordings. First, body parts were tracked using LEAP. These postures were then processed, as described in Klibaite et al. 2022, to assign one of six behaviors to each time point in the recording. Locomotion was divided into slow, medium and fast based on the centroid velocity of the mouse. (C) The probability to be in the fast locomotion state decreased within and across days for the CNO only control group, but lobule VI-perturbed mice show a higher or similar probability to be in fast locomotion at the beginning of the experiment on the second day compared to the first day. (D) The state occupancies for lobule VI-perturbed mice changed less across days than the other groups, indicating a lack of adaptation. (E) The state transitions for lobule VI-perturbed mice changed less across days than control group, indicating a lack of adaptation. *** $p < 0.001$

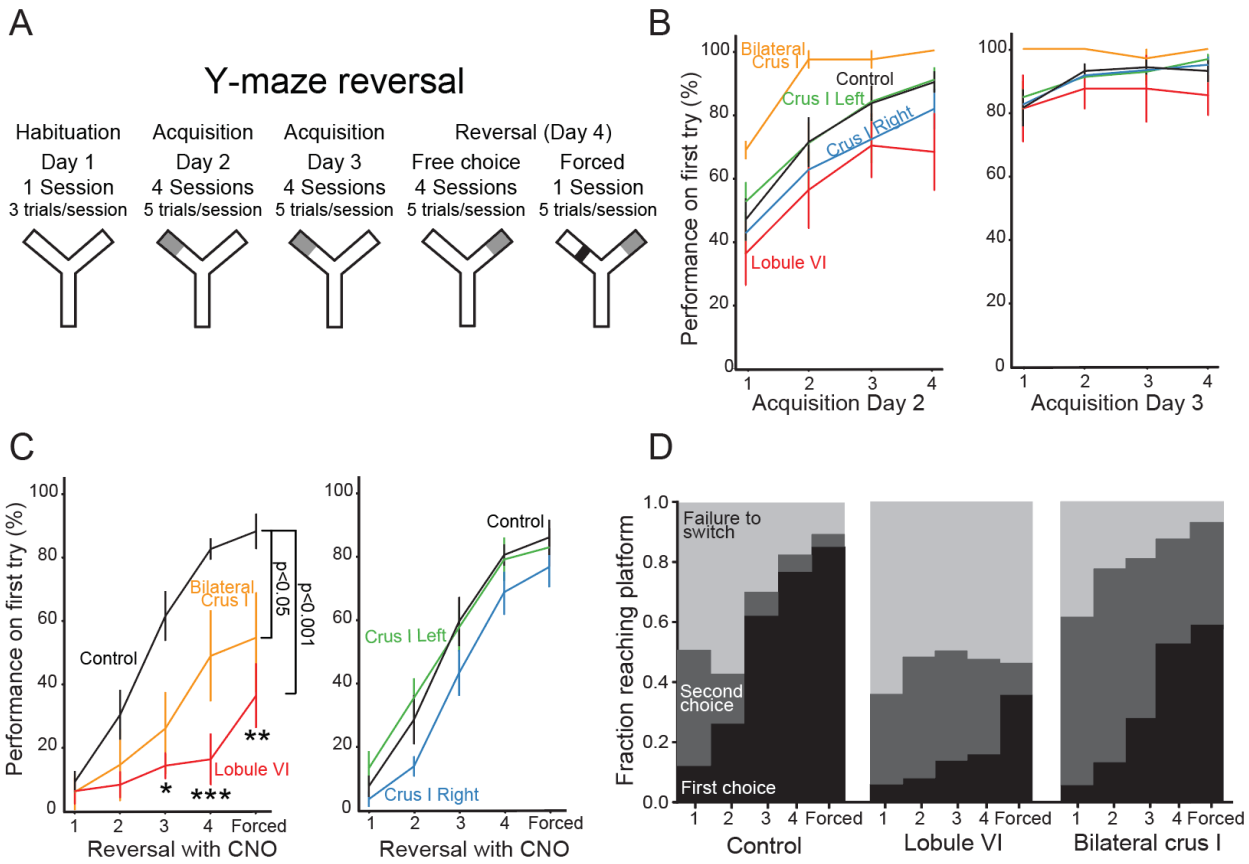

Figure 3. Effect of lobule VI and crus I inactivation on behavior. (A) Protocol for Y-maze reversal consisting of habituation, two days of training (day 2 and day 3), and one reversal day ending in a forced session (day 4). (B) Animals learned to find the platform over two days. First try performance of 80% at the end of session 4 was required to continue to reversal. (C) Y-maze reversal was impaired in animals with lobule VI and bilateral crus I (left) inactivation compared to CNO only control. Unilateral effects were not found (right) compared to controls. (D) Typical mice learned through trial and error, demonstrating more accurate performance over time. Lobule VI and crus I perturbed mice stayed repeatedly with the original incorrect choice compared to CNO only control. Error bars indicate mean ± SEM. Comparisons were made using a generalized mixed effect model (GLMM) with a binomial distribution. * $p < 0.05$, ** $p < 0.01$, *** $p < 0.001$

`

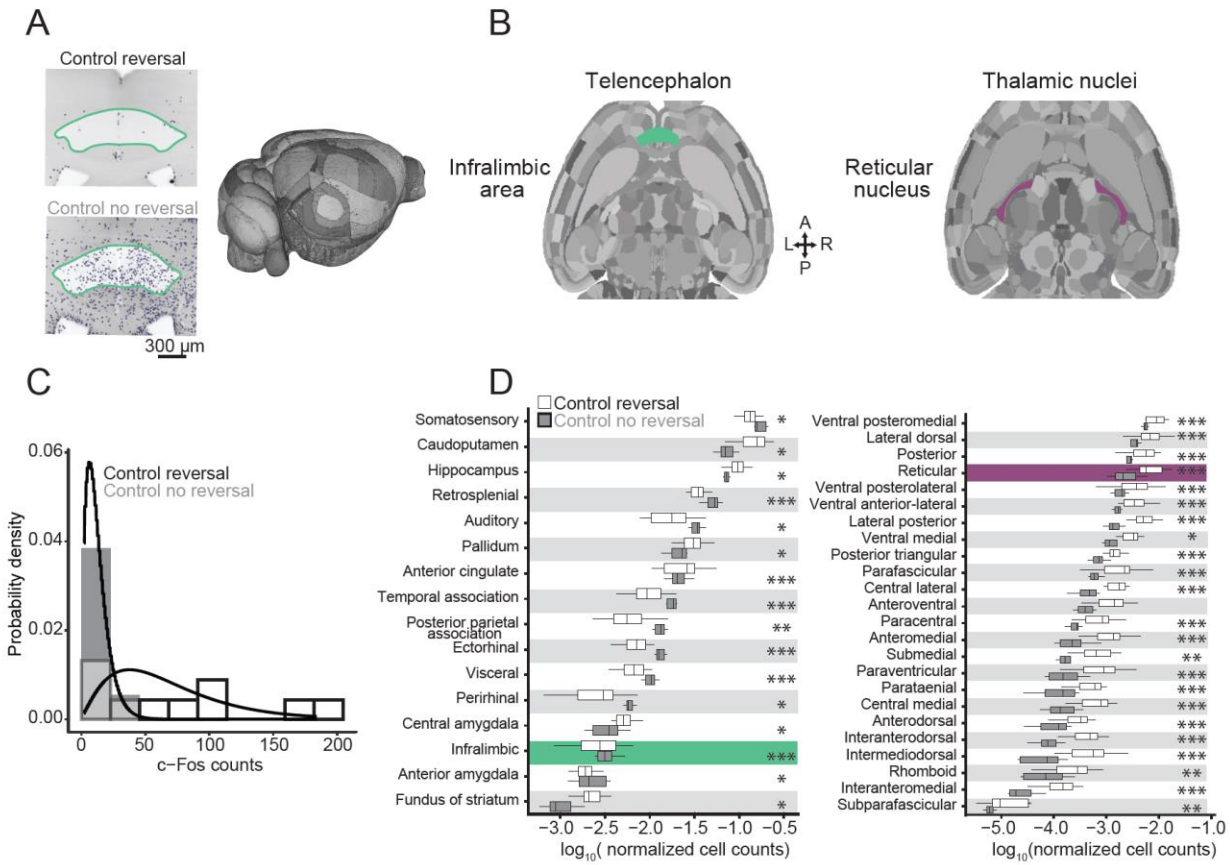

Figure 4. Whole-brain analysis of c-Fos in CNO only controls. (A) Example of ClearMap cell counting in the infralimbic area in CNO only reversal compared to CNO only no reversal (left). Neuroglancer 3-D mouse brain (right). (B) Example horizontal mouse brain sections representing infralimbic area (green) and reticular nucleus (purple). (C) Negative binomial regression under two CNO only controls undergoing reversal or no reversal. This example, nucleus raphe pontis. Nonparametric kernel density estimates derived from count-based densities (bars). Solid curves indicate the probabilities at each count level from a fitted negative binomial regression model. (D) Normalized cell counts (log_{10}) in the telencephalon (left) and thalamus (right) comparing CNO only reversal (white) and no reversal (gray). Comparisons were made using a negative binomial regression. * $p < 0.05$, ** $p < 0.01$, *** $p < 0.001$

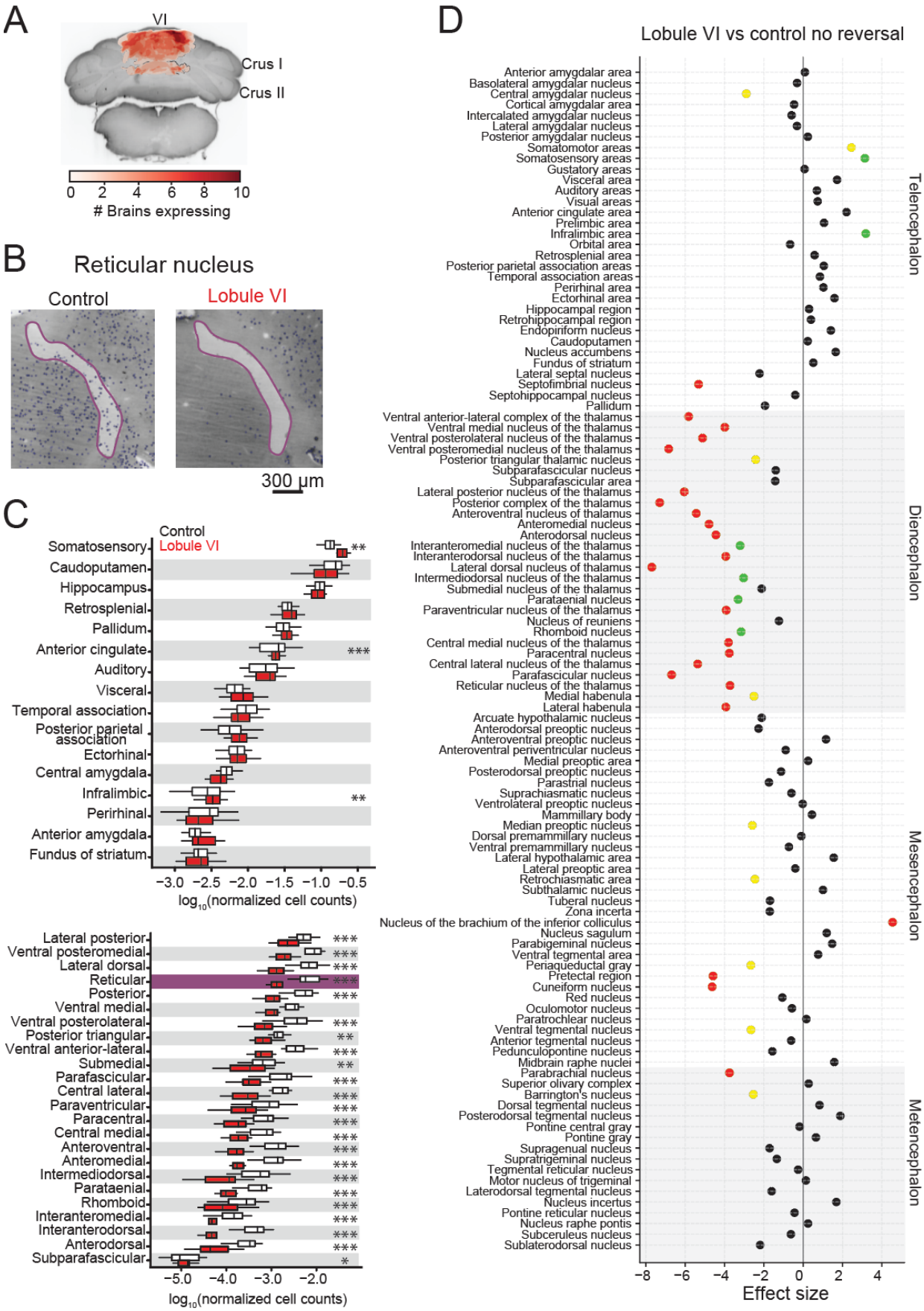
A
VI
Crus I
Crus II
0 2 4 6 8 10
Brains expressing
B
Reticular nucleus
Control
Lobule VI
300 µm
C
Control
Lobule VI
Somatosensory
Caudoputamen
Hippocampus
Retrosplenial
Pallidum
Anterior cingulate
Auditory
Visceral
Temporal association
Posterior parietal association
Ectorhinal
Central amygdala
Infralimbic
Perirhinal
Anterior amygdala
Fundus of striatum
−3.0 −2.5 −2.0 −1.5 −1.0 −0.5
log10(normalized cell counts)
Lateral posterior
Ventral posteromedial
Lateral dorsal
Reticular
Posterior
Ventral medial
Ventral posterolateral
Posterior triangular
Ventral anterior-lateral
Submedial
Parafascicular
Central lateral
Paraventricular
Paracentral
Central medial
Anteroventral
Anteromedial
Intermediodorsal
Parataenial
Rhomboid
Interanteromedial
Interanterodorsal
Anterodorsal
Subparafascicular
−5.0 −4.0 −3.0 −2.0
log10(normalized cell counts)
D
Lobule VI vs control no reversal
Anterior amygdalar area
Basolateral amygdalar nucleus
Central amygdalar nucleus
Cortical amygdalar area
Intercalated amygdalar nucleus
Lateral amygdalar nucleus
Posterior amygdalar nucleus
Somatomotor areas
Somatosensory areas
Gustatory areas
Visceral area
Auditory areas
Visual areas
Anterior cingulate area
Prelimbic area
Infralimbic area
Orbital area
Retrosplenial area
Posterior parietal association areas
Temporal association areas
Perirhinal area
Ectorhinal area
Hippocampal region
Retrohippocampal region
Endopiriform nucleus
Caudoputamen
Nucleus accumbens
Fundus of striatum
Lateral septal nucleus
Septofimbrial nucleus
Septohippocampal nucleus
Pallidum
Ventral anterior-lateral complex of the thalamus
Ventral medial nucleus of the thalamus
Ventral posterolateral nucleus of the thalamus
Ventral posteromedial nucleus of the thalamus
Posterior triangular thalamic nucleus
Subparafascicular nucleus
Subparafascicular area
Lateral posterior nucleus of the thalamus
Posterior complex of the thalamus
Anteroventral nucleus of thalamus
Anteromedial nucleus
Anterodorsal nucleus
Interanteromedial nucleus of the thalamus
Interanterodorsal nucleus of the thalamus
Lateral dorsal nucleus of thalamus
Intermediodorsal nucleus of the thalamus
Submedial nucleus of the thalamus
Parataenial nucleus
Paraventricular nucleus of the thalamus
Nucleus of reuniens
Rhomboid nucleus
Central medial nucleus of the thalamus
Paracentral nucleus
Central lateral nucleus of the thalamus
Parafascicular nucleus
Reticular nucleus of the thalamus
Medial habenula
Lateral habenula
Arcuate hypothalamic nucleus
Anterodorsal preoptic nucleus
Anteroventral preoptic nucleus
Anteroventral periventricular nucleus
Medial preoptic area
Posterodorsal preoptic nucleus
Parastrial nucleus
Suprachiasmatic nucleus
Ventrolateral preoptic nucleus
Mammillary body
Median preoptic nucleus
Dorsal premammillary nucleus
Ventral premammillary nucleus
Lateral hypothalamic area
Lateral preoptic area
Retrochiasmatic area
Subthalamic nucleus
Tuberal nucleus
Zona incerta
Nucleus of the brachium of the inferior colliculus
Nucleus sagulum
Parabigeminal nucleus
Ventral tegmental area
Periaqueductal gray
Pretectal region
Cuneiform nucleus
Red nucleus
Oculomotor nucleus
Paratrochlear nucleus
Ventral tegmental nucleus
Anterior tegmental nucleus
Pedunculopontine nucleus
Midbrain raphe nuclei
Parabrachial nucleus
Superior olivary complex
Barrington's nucleus
Dorsal tegmental nucleus
Posterodorsal tegmental nucleus
Pontine central gray
Pontine gray
Supragenual nucleus
Supratrigeminal nucleus
Tegmental reticular nucleus
Motor nucleus of trigeminal
Laterodorsal tegmental nucleus
Nucleus incertus
Pontine reticular nucleus
Nucleus raphe pontis
Subceruleus nucleus
Sublaterodorsal nucleus
Telencephalon
Diencephalon
Mesencephalon
Metencephalon
−8 −6 −4 −2 0 2 4
Effect size

Figure 5. Effects of Lobule VI perturbation on whole-brain c-Fos. (A) Overlay of regions of DREADD-AAV expression recovered using immunofluorescent labeling of mCherry and lightsheet microscopy imaging. (B) Example images of ClearMap cell counting in the reticular nucleus comparing Lobule VI and CNO only control after reversal. (C) Normalized cell counts ($\log_{10}$) by total regions analyzed in the telencephalon (top) and thalamus (bottom) comparing Lobule VI and CNO only after reversal. (D) Statistically-significant ($p < 0.05$) lobule VI reversal versus lobule VI control no reversal. Lobule VI perturbation modulated regions necessary for reversal learning, including thalamus. Comparisons were made using a negative binomial regression. Yellow: * $p < 0.05$, Green: ** $p < 0.01$, Red: *** $p < 0.001$

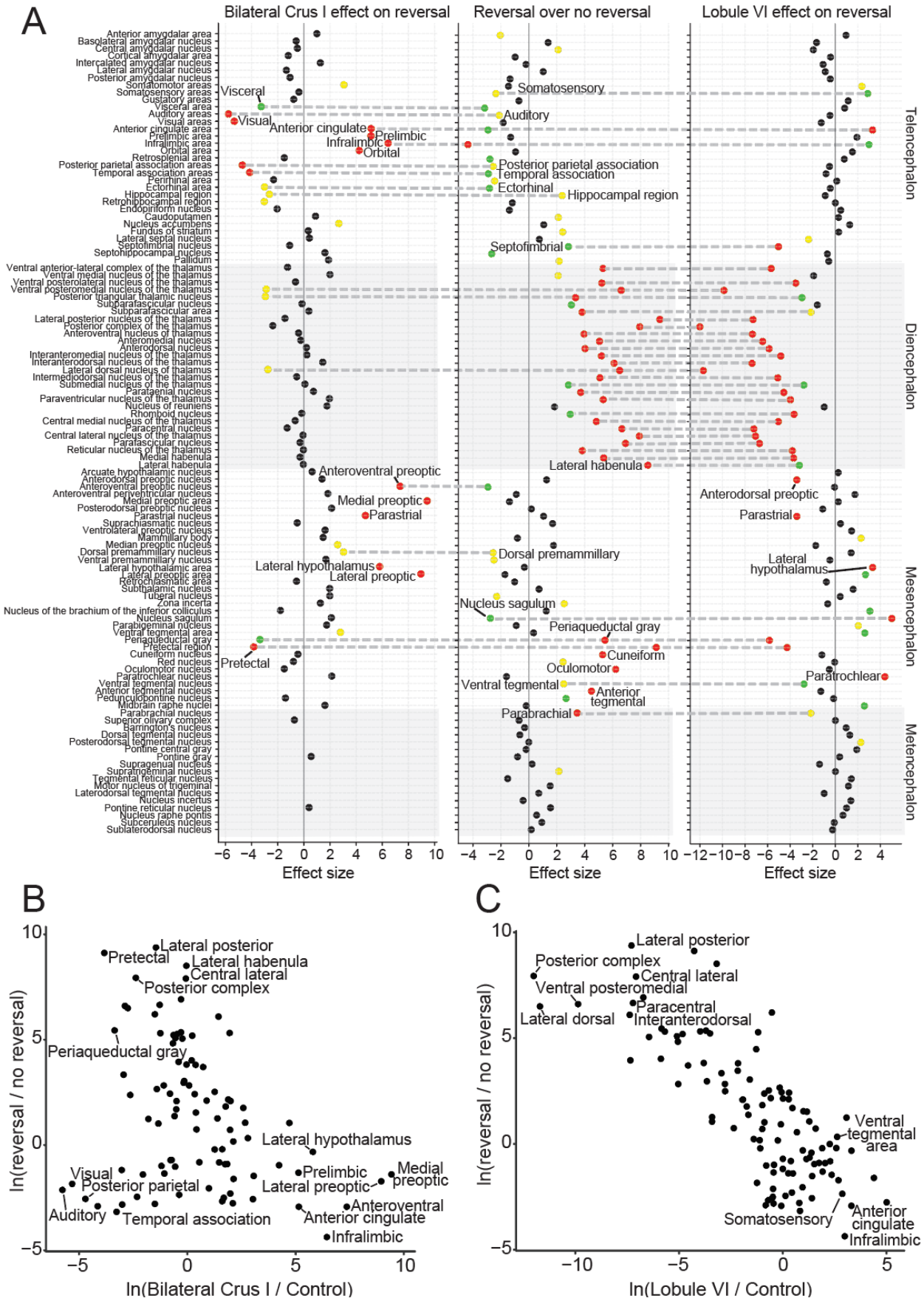
A
Bilateral Crus I effect on reversal
Reversal over no reversal
Lobule VI effect on reversal
Telencephalon
Diencephalon
Mesencephalon
Metencephalon
Visceral
Visual
Anterior cingulate
Prelimbic
Infralimbic
Orbital
Somatosensory
Auditory
Posterior parietal association
Temporal association
Ectorhinal
Hippocampal region
Septofimbrial
Lateral habenula
Anteroventral preoptic
Medial preoptic
Parastrial
Anterodorsal preoptic
Lateral hypothalamus
Lateral preoptic
Dorsal premammillary
Nucleus sagulum
Periaqueductal gray
Pretectal
Cuneiform
Oculomotor
Paratrochlear
Ventral tegmental
Anterior tegmental
Parabrachial
Effect size
B
Lateral posterior
Pretectal
Lateral habenula
Central lateral
Posterior complex
Periaqueductal gray
Lateral hypothalamus
Visual
Posterior parietal
Prelimbic
Medial preoptic
Lateral preoptic
Auditory
Temporal association
Anteroventral
Anterior cingulate
Infralimbic
ln(reversal / no reversal)
ln(Bilateral Crus I / Control)
C
Lateral posterior
Posterior complex
Central lateral
Ventral posteromedial
Paracentral
Lateral dorsal
Interanterodorsal
Ventral tegmental area
Somatosensory
Anterior cingulate
Infralimbic
ln(reversal / no reversal)
ln(Lobule VI / Control)

Figure 6. Brain-wide association study to identify activated regions of c-Fos expression. (A) Statistically-significant ($p < 0.05$) bilateral crus I (left), reversal (middle) lobule VI (right) structures compared to CNO only controls. Lobule VI (right) perturbation modulated regions necessary for reversal learning, including thalamus and anterior cingulate cortex. Crus I bilateral (left) perturbation altered regions in the telencephalon, including prelimbic, infralimbic, anterior cingulate, and orbital frontal cortex (B) Correlations between crus I and reversal learning structures (Pearson's $r = -0.29$). (C) A strong negative correlation was found between lobule VI and reversal learning structures (Pearson's $r = -0.78$). All data were calculated as the natural log of ratios rescaled by the standard error. Comparisons were made using a negative binomial regression. Bilateral Crus I and lobule VI were compared to CNO only controls. Yellow: $p < 0.05$, Green: $p < 0.01$, Red: $p < 0.001$

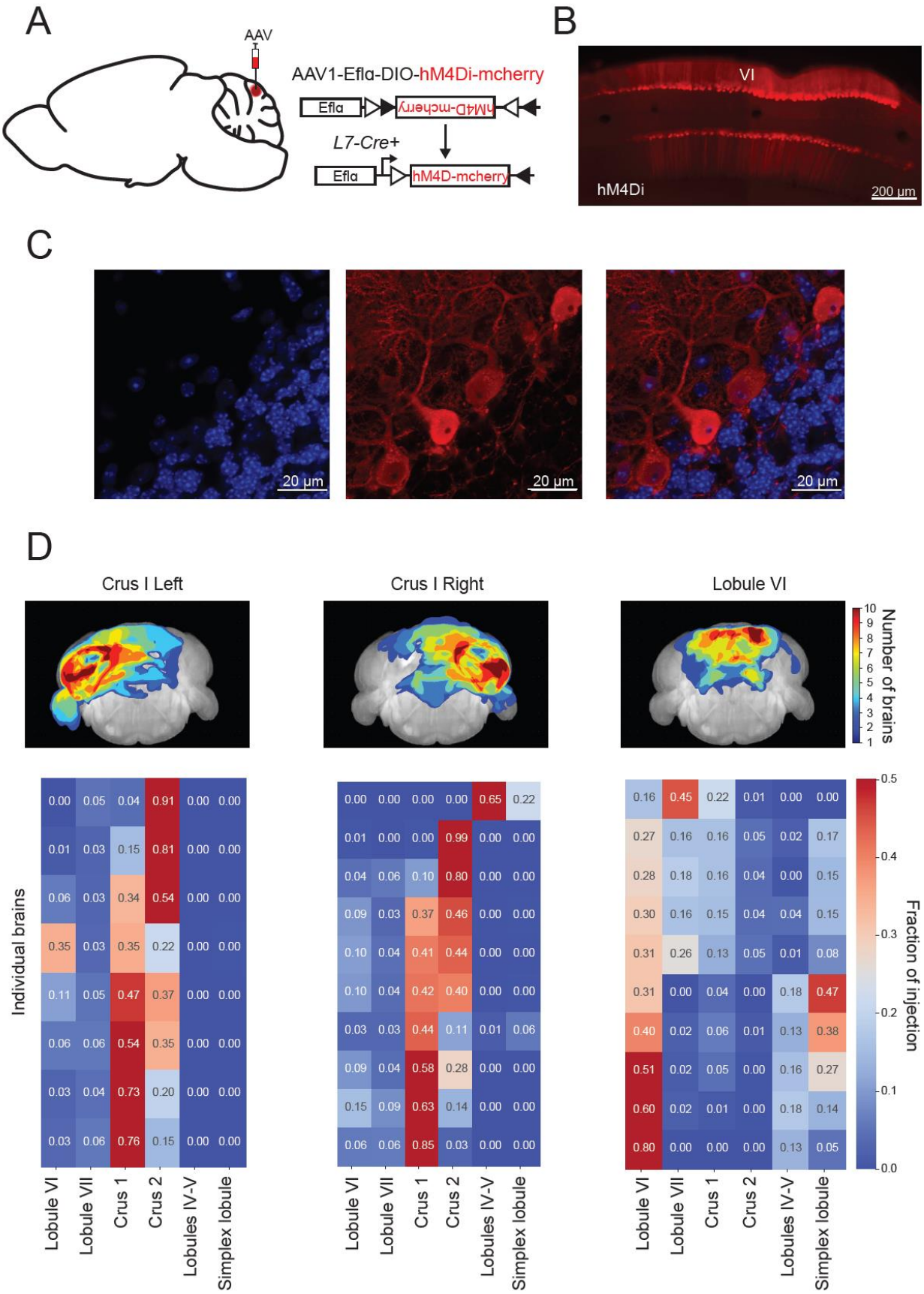
A
AAV
AAV1-Efla-DIO-hM4Di-mcherry
Efla
hM4D-mcherry
L7-Cre+
Efla
hM4D-mcherry
B
VI
hM4Di
200 µm
C
20 µm
20 µm
20 µm
D
Crus I Left
Crus I Right
Lobule VI
Number of brains
Individual brains
Fraction of injection
Lobule VI
Lobule VII
Crus 1
Crus 2
Lobules IV-V
Simplex lobule

Figure 1-figure supplement 1. Selective expression of mCherry in Purkinje cells of the cerebellum. (A) AAV carrying hM4Di fused to mCherry was injected into lobule VI or crus I of C57BL/6J mice along with AAV-L7-cre virus to allow for Purkinje cell-specific expression. (B) Sagittal section showing fluorescent expression (epifluorescent images at 40x) revealed by anti-RFP immunohistochemistry 3 weeks after injection in lobule VI. (C) Immunostaining confocal fluorescent images (63x) of lobule VI reveal hM4Di-mCherry expression in Purkinje cells. (D) Top: Whole-brain lightsheet averaged injection volumes calculated based on immunostaining of mCherry. Bottom: Calculated subset of individual brain volumes of the DREADD fraction injected per cerebellar lobule of interest.

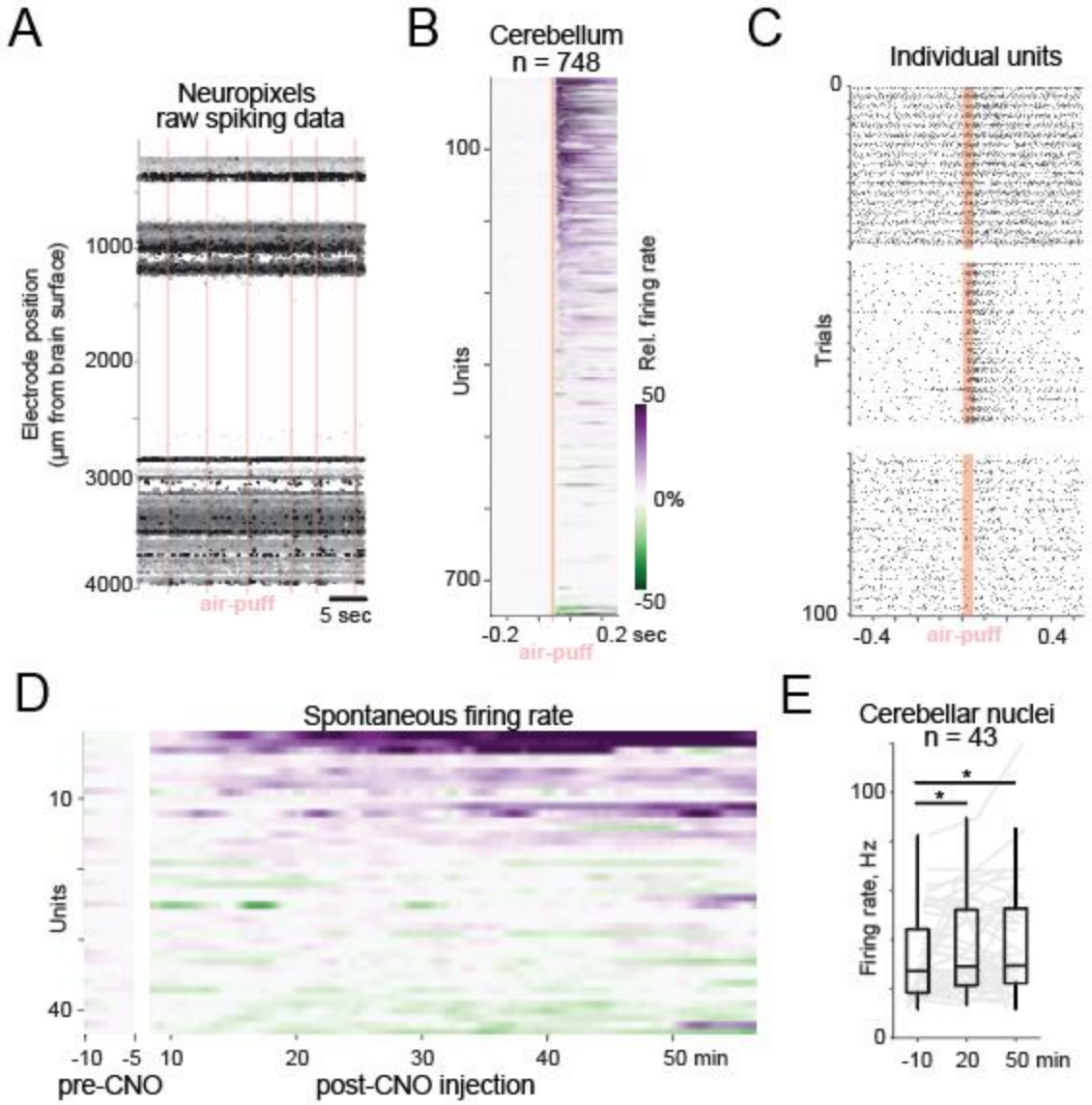

Figure 1-figure supplement 2. Neuropixels recordings of DREADD-expression in Purkinje cells. (A) Raw spiking data on all 384 electrodes of the probe placed in cerebellum during a sensory stimulation with air puff. Stimulus time (40 ms, 1 pulse) is indicated with a red bar. (B) Normalized averaged responses of all sorted units to an air-puff stimulation. (C) Raster of spikes for 100 repetitions of the air-puff stimulation for three example units. Stimulus time (40 ms, 1 pulse) is indicated with a red bar. (D) Spontaneous firing rate of deep cerebellar nuclei neurons before and after CNO injection to mice with Purkinje cells expressing DREADD receptors. (E) Individual and average spontaneous firing rate of deep cerebellar nuclei neurons increases over 50 min after activation of DREADD receptors in Purkinje cells.

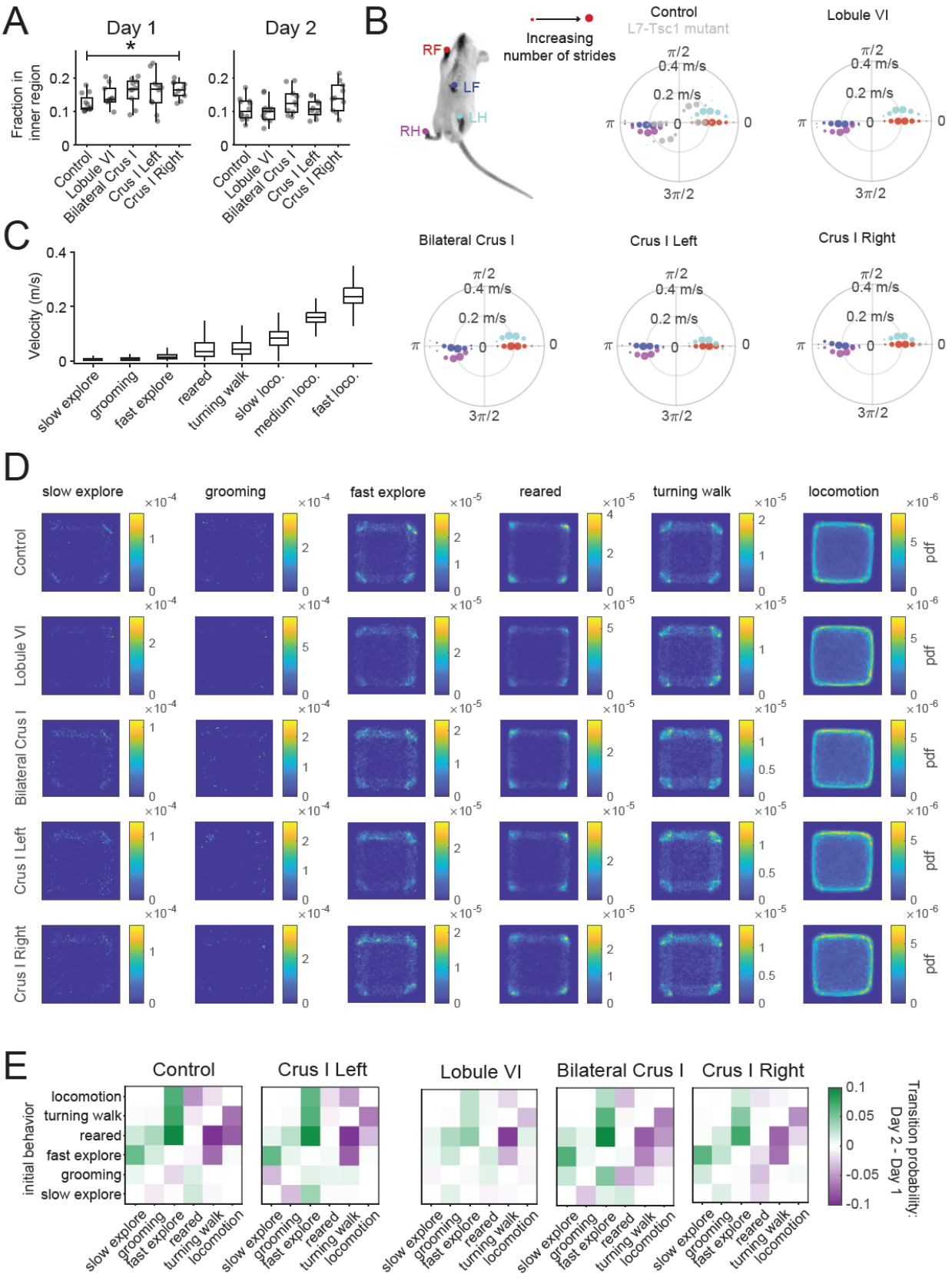
A
Day 1
Day 2
Fraction in inner region
Control
Lobule VI
Bilateral Crus I
Crus I Left
Crus I Right
B
RF
LF
LH
RH
Increasing number of strides
Control
L7-Tsc1 mutant
Lobule VI
Bilateral Crus I
Crus I Left
Crus I Right
0.4 m/s
0.2 m/s
C
Velocity (m/s)
slow explore
grooming
fast explore
reared
turning walk
slow loco.
medium loco.
fast loco.
D
slow explore
grooming
fast explore
reared
turning walk
locomotion
pdf
E
initial behavior
locomotion
turning walk
reared
fast explore
grooming
slow explore
Transition probability: Day 2 - Day 1

Figure 2-figure supplement 1. Lobule-specific alterations of spontaneous behavior in open field. (A) Fraction of time spent in the inner region of the arena. Comparisons of the groups within each day to CNO only control were made using a Kruskal-Wallis test, followed up by pairwise comparisons using Wilcoxon rank sum exact tests with Benjamini-Hochberg correction. (B) Limb coordination during locomotion is not impaired by cerebellar perturbations. The maximal values of the paw positions in an animal-centered coordinate system were assumed at similar phases during single strides of locomotion. For comparison altered limb coordination in L7-Tsc1 mutant mice is shown from previously published experiments (Klibaite et al., 2022). (C) Centroid velocities during different behaviors. (D) The spatial distributions of occurrences of the different behaviors in the open field arena are similar for each experimental group compared to CNO only control. Data from the recording on day 1 was considered. (E) Lobule VI-perturbed CNO only control mice showed the smallest differences in the state transition probabilities across days. * $p < 0.05$

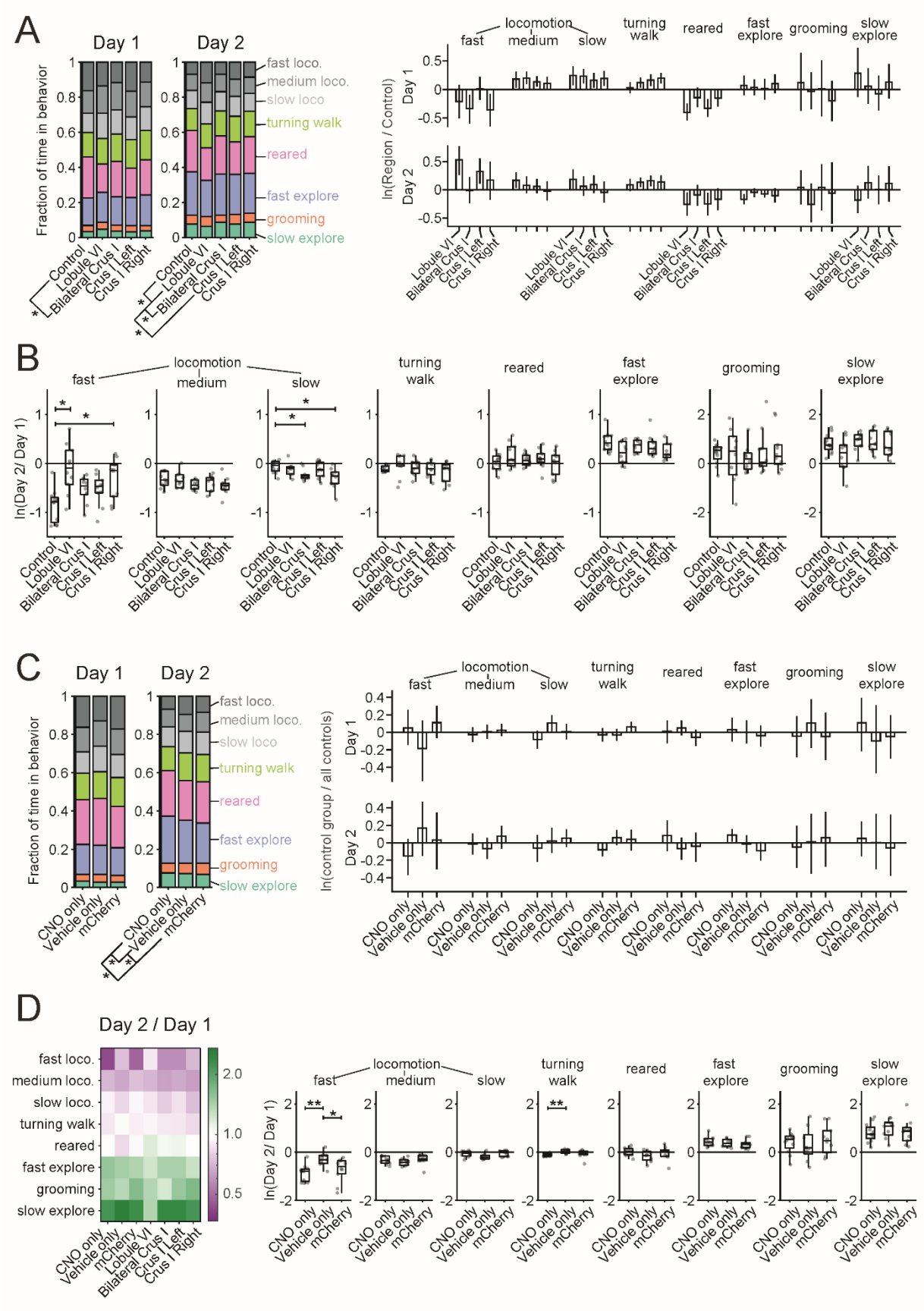
A
Day 1
Day 2
Fraction of time in behavior
fast loco.
medium loco.
slow loco
turning walk
reared
fast explore
grooming
slow explore
Control
Lobule VI
Bilateral Crus I
Crus I Left
Crus I Right
locomotion
fast
medium
slow
turning walk
reared
fast explore
grooming
slow explore
ln(Region / Control)
Day 1
Day 2
B
ln(Day 2/ Day 1)
C
ln(control group / all controls)
CNO only
Vehicle only
mCherry
D
Day 2 / Day 1

Figure 2-figure supplement 2. Comparison of spontaneous behavior in control groups. (A) The fractions of time spent in each of the eight behaviors (compositional means) differ significantly between lobule VI-perturbed mice and the CNO only control group on day 2 (nonparametric multivariate test on ilr-transformed fractions, ssnonpartest from R package npmv, Wilks' Lambda type statistic). This difference can be mainly accounted for by the large amount of time spent in fast locomotion on the second day compared to the control, quantified by the log ratio differences between the cerebellar perturbed groups and the control (error bars indicate bootstrapped 95% confidence intervals, N = 5000, percentile bootstrap) (B) Cerebellar perturbations of lobule VI, crus I right and bilateral crus I had an effect on the adaptation of the occupancy in slow and fast locomotion states across days compared to CNO only control (Kruskal-Wallis tests for each behavior, pairwise comparisons using Wilcoxon rank sum exact test, Benjamini-Hochberg correction). (C) Same as in A for mice without a cerebellar perturbation given CNO on day 1 (CNO only), mice without a cerebellar perturbation given vehicle only on day 1 (vehicle only), and mice that received AAV with mCherry only and CNO on day 1 (mCherry). The control groups show significant differences on day 2 (nonparametric multivariate test on ilr-transformed fractions, ssnonpartest from R package npmv, Wilks' Lambda type statistic). (D) All control groups show a similar change of behavioral occupancies across days. Mice that received vehicle only showed a difference in adaptation of fast locomotion and turning walk across days compared to CNO only (Kruskal-Wallis tests for each behavior, pairwise comparisons using Wilcoxon rank sum exact test, Benjamini-Hochberg correction). * $p < 0.05$, ** $p < 0.01$

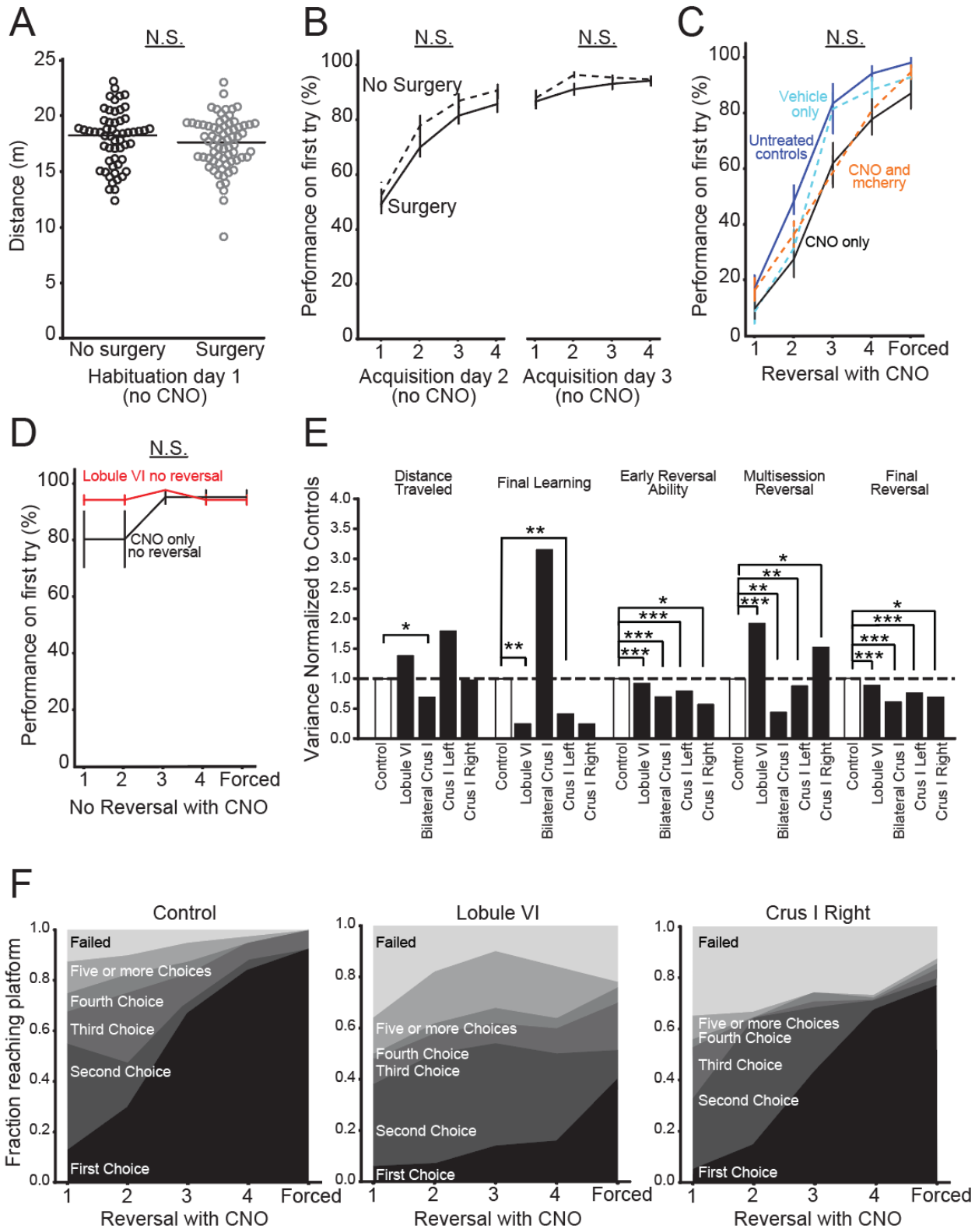
A
N.S.
Distance (m)
No surgery
Surgery
Habituation day 1
(no CNO)
B
N.S.
N.S.
Performance on first try (%)
No Surgery
Surgery
Acquisition day 2
(no CNO)
Acquisition day 3
(no CNO)
C
N.S.
Performance on first try (%)
Vehicle only
Untreated controls
CNO and mcherry
CNO only
Forced
Reversal with CNO
D
N.S.
Lobule VI no reversal
CNO only no reversal
Performance on first try (%)
Forced
No Reversal with CNO
E
Distance Traveled
Final Learning
Early Reversal Ability
Multisession Reversal
Final Reversal
Variance Normalized to Controls
Control
Lobule VI
Bilateral Crus I
Crus I Left
Crus I Right
F
Control
Lobule VI
Crus I Right
Fraction reaching platform
Failed
Five or more Choices
Fourth Choice
Third Choice
Second Choice
First Choice
Forced
Reversal with CNO

Figure 3-figure supplement 1. Additional Y-maze metrics. (A) Surgery (DREADD experimental conditions and mCherry) had no effect on swimming total distance during habituation compared to no surgery (Untreated, Vehicle only, CNO only). (B) All animals were taught to swim to one single side of the Y-maze during acquisition sessions. Surgery had no effect on acquisition day 1 or 2. (C) To control for the unintended consequences of CNO, mice were given CNO or vehicle 20 minutes before testing. To control for potential AAV effects, animals received AAV with mCherry only and CNO during testing. No effects from AAV, CNO, or vehicle were found. (D) To test if activating the DREADD virus in lobule VI perturbed acquisition, a separate group of lobule VI mice were tested using a third acquisition day (no reversal) and compared to a CNO only no reversal group. No effects of CNO or DREADD perturbation were found in the no reversal condition. (E) Variance in distance traveled is less than during learning and reversal within experimental groups compared to untreated controls. (F) The number of choices required to find the platform in the Y-maze comparing experimental groups to CNO only control. Comparisons were made using one or two-way repeated measures ANOVA. Error bars indicate mean ± SEM. * $p < 0.05$, ** $p < 0.01$, *** $p < 0.001$

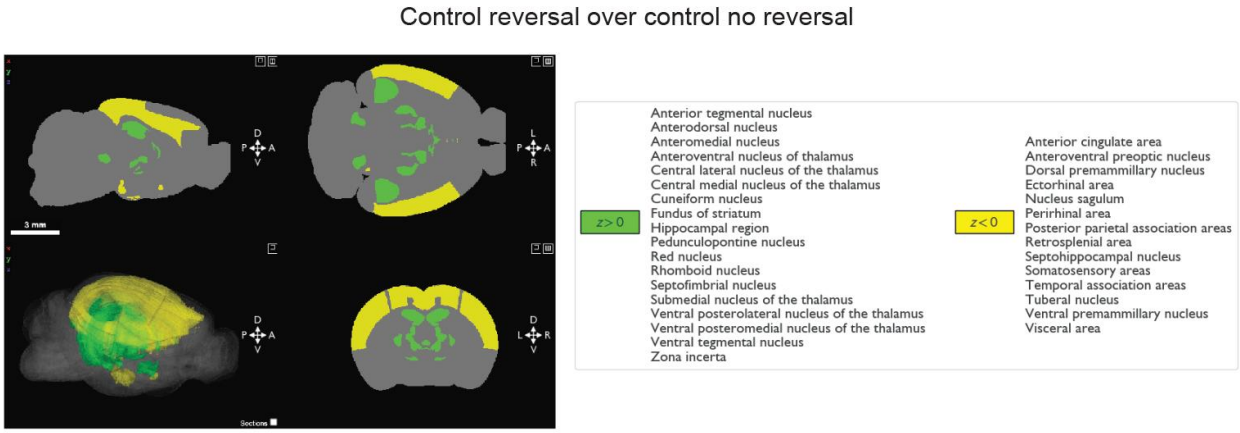

Figure 4-figure supplement 1. Reversal learning alters region-specific activity. Whole-brain Neuroglancer visualization of significantly different regions in CNO only reversal compared to no reversal controls. Reversal resulted in different activated brain regions compared to acquisition. Green: increases, $p < 0.05$, Yellow: decreases, $p < 0.05$

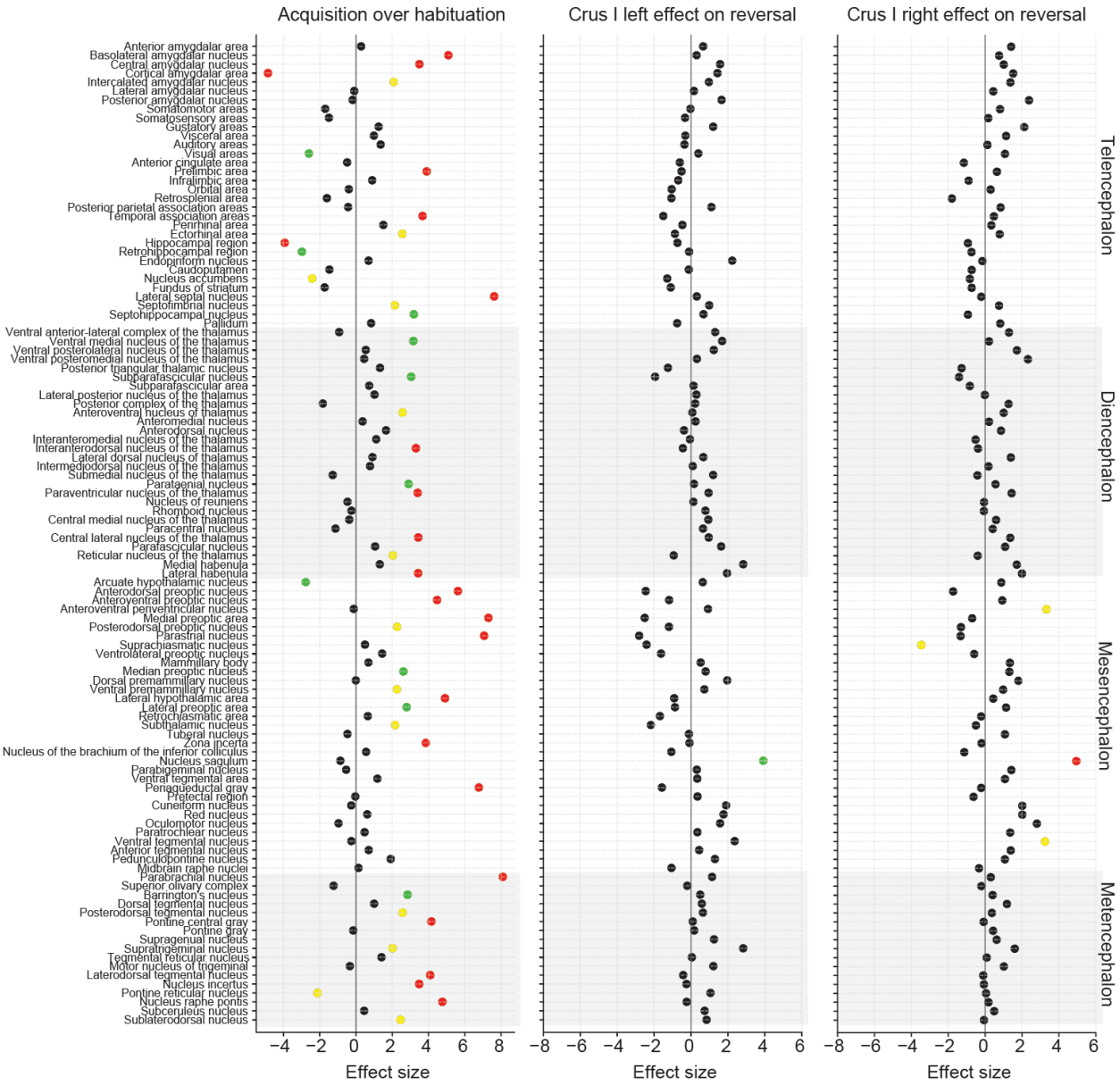

Figure 5-figure supplement 1. Additional comparisons from whole-brain imaging of c-Fos. (Left) Comparisons between acquisition only and habituation only groups are plotted by effect size differences to find structures activated by the acquisition condition. Unilateral crus I left (middle) and crus I right (right) perturbation had little effect on c-Fos cell counts compared to CNO only control, which is consistent with a lack of a behavioral effect during reversal in the water Y-maze task. Comparisons were made using a negative binomial regression.Yellow: $p < 0.05$, Green: $p < 0.01$, Red: $p < 0.001$

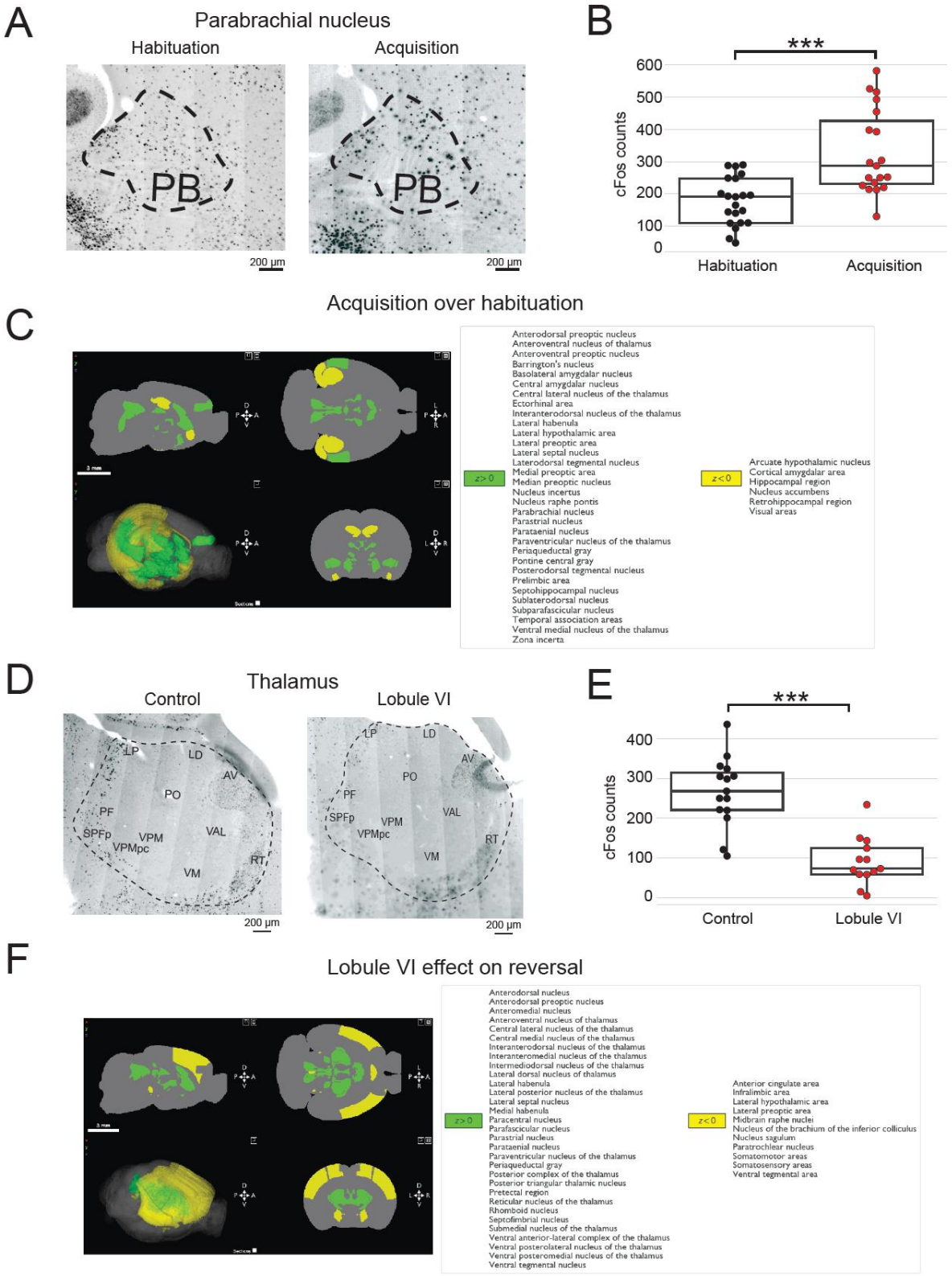
A
Parabrachial nucleus
Habituation
Acquisition
PB
PB
200 µm
200 µm
B
***
cFos counts
600
500
400
300
200
100
0
Habituation
Acquisition
C
Acquisition over habituation
z > 0
Anterodorsal preoptic nucleus
Anteroventral nucleus of thalamus
Anteroventral preoptic nucleus
Barrington's nucleus
Basolateral amygdalar nucleus
Central amygdalar nucleus
Central lateral nucleus of the thalamus
Ectorhinal area
Interanterodorsal nucleus of the thalamus
Lateral habenula
Lateral hypothalamic area
Lateral preoptic area
Lateral septal nucleus
Laterodorsal tegmental nucleus
Medial preoptic area
Median preoptic nucleus
Nucleus incertus
Nucleus raphe pontis
Parabrachial nucleus
Parastrial nucleus
Parataenial nucleus
Paraventricular nucleus of the thalamus
Periaqueductal gray
Pontine central gray
Posterodorsal tegmental nucleus
Prelimbic area
Septohippocampal nucleus
Sublaterodorsal nucleus
Subparafascicular nucleus
Temporal association areas
Ventral medial nucleus of the thalamus
Zona incerta
z < 0
Arcuate hypothalamic nucleus
Cortical amygdalar area
Hippocampal region
Nucleus accumbens
Retrohippocampal region
Visual areas
D
Thalamus
Control
Lobule VI
LP
LD
AV
PO
PF
SPFp
VPM
VPMpc
VAL
RT
VM
200 µm
200 µm
E
***
cFos counts
400
300
200
100
0
Control
Lobule VI
F
Lobule VI effect on reversal
z > 0
Anterodorsal nucleus
Anterodorsal preoptic nucleus
Anteromedial nucleus
Anteroventral nucleus of thalamus
Central lateral nucleus of the thalamus
Central medial nucleus of the thalamus
Interanterodorsal nucleus of the thalamus
Interanteromedial nucleus of the thalamus
Intermediodorsal nucleus of the thalamus
Lateral dorsal nucleus of thalamus
Lateral habenula
Lateral posterior nucleus of the thalamus
Lateral septal nucleus
Medial habenula
Paracentral nucleus
Parafascicular nucleus
Parastrial nucleus
Parataenial nucleus
Paraventricular nucleus of the thalamus
Periaqueductal gray
Posterior complex of the thalamus
Posterior triangular thalamic nucleus
Pretectal region
Reticular nucleus of the thalamus
Rhomboid nucleus
Septofimbrial nucleus
Submedial nucleus of the thalamus
Ventral anterior-lateral complex of the thalamus
Ventral posterolateral nucleus of the thalamus
Ventral posteromedial nucleus of the thalamus
Ventral tegmental nucleus
z < 0
Anterior cingulate area
Infralimbic area
Lateral hypothalamic area
Lateral preoptic area
Midbrain raphe nuclei
Nucleus of the brachium of the inferior colliculus
Nucleus sagulum
Paratrochlear nucleus
Somatomotor areas
Somatosensory areas
Ventral tegmental area

Figure 6-figure supplement 1. Acquisition and lobule VI perturbation activate an unique set of brain regions in the water Y-maze task. (A) Conventional immunohistochemical staining of c-Fos in the parabrachial nucleus (PB) in habituation only versus acquisition only groups. (B) Acquisition only mice had increased c-Fos staining in PB. Scale bar 200 (C) Whole-brain Neuroglancer visualization of significantly different regions in acquisition circuits. (D) Conventional immunohistochemical staining of c-Fos in the thalamus of Lobule VI compared to CNO only. Lateral posterior nucleus (LP), lateral dorsal nucleus (LD), anteroventral nucleus (AV), posterior complex (PO), ventral anterior-lateral complex (VAL), ventral medial nucleus (VM), reticular nucleus (RT), ventral posteromedial nucleus (VPM), ventral posteromedial nucleus parvicellular part (VPMpc), subparafascicular parvicellular part (SPFp), parafascicular nucleus (PF). (E) Lobule VI mice had significantly less c-Fos in thalamic regions compared to CNO only. (F) Whole-brain Neuroglancer visualization of significantly different regions in lobule VI circuits. Green: increases, $p < 0.05$, Yellow: decreases, $p < 0.05$, *** $p < 0.001$

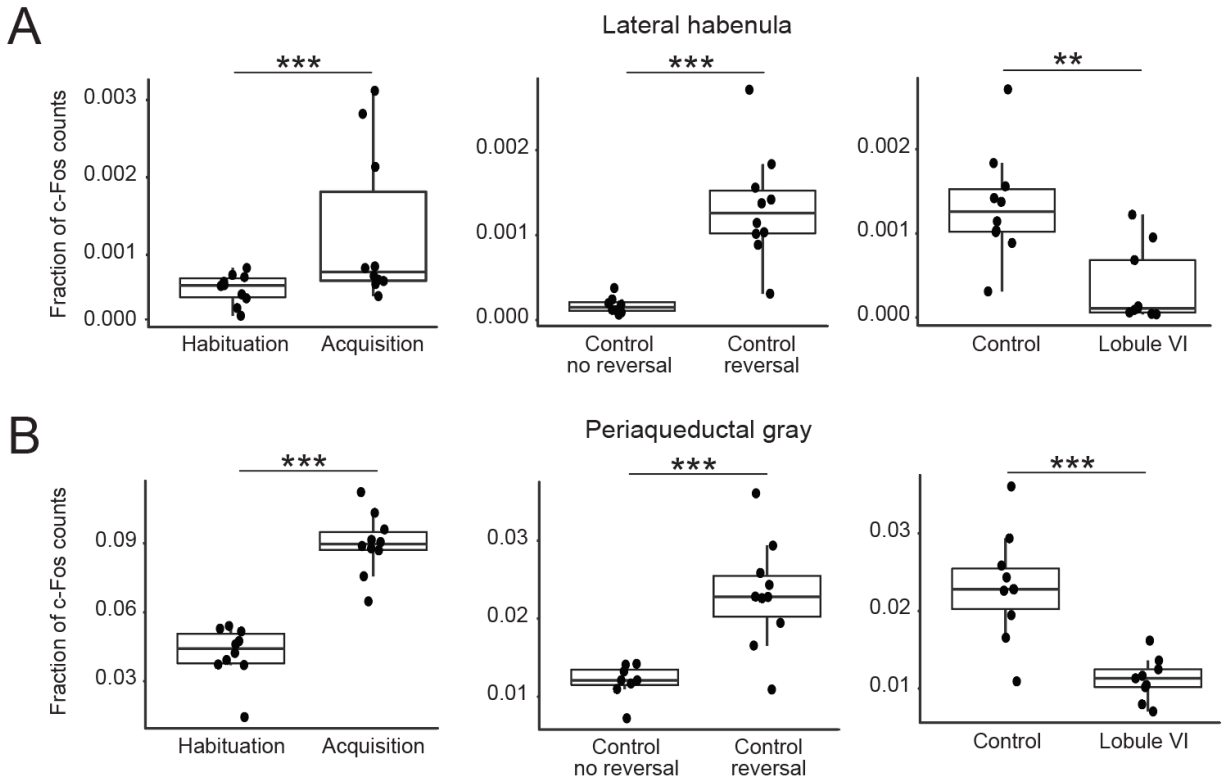

Figure 6-figure supplement 2. c-Fos neural activation in lateral habenula and periaqueductal gray. (A) Y-maze acquisition (left) and reversal learning in CNO only controls (middle) significantly increased c-Fos in the lateral habenula. Lobule VI perturbation reduced c-Fos counts in the lateral habenula compared to reversal learning (right). (B) In periaqueductal gray, (B) In the periaqueductal gray, Y-maze acquisition (left) and reversal learning in CNO only controls (middle) significantly increased c-Fos counts. Lobule VI perturbation reduced c-Fos counts in the periaqueductal gray compared to reversal learning (right). Comparisons were made using a pairwise t-test. ** $p < 0.01$, *** $p < 0.001$

Control group	Experimental group	Figure
	Lobule VI	Fig 1C-G, Fig 1 S1B-C, Fig 1 S2A-D
CNO only	Lobule VI	Fig 2A (left) and C and E, Fig 5B-C, Fig 6 S1D-F
CNO only	Lobule VI, Bilateral Crus I, Crus I Left, Crus I Right	Fig 2A (right), Fig 2D, Fig 3B, Fig 2 S1A-B and D-E, Fig 2 S2A-B
CNO only	Lobule VI, Bilateral Crus I	Fig 3C (left)-D
CNO only	Crus I Left, Crus I Right	Fig 3C (right)
CNO only, CNO only no reversal		Fig 4A and C-D, Fig 4 S1
Lobule VI no reversal	Lobule VI reversal	Fig 5D
CNO only, CNO only no reversal	Lobule VI, Bilateral Crus I	Fig 6A-B
CNO only, CNO only no reversal	Lobule VI	Fig 6C
	Lobule VI, Crus I Left, Crus I Right	Fig 1 S1D
CNO only, Vehicle only, mCherry		Fig 2 S2C and D (right)
CNO only, Vehicle only, mCherry	Lobule VI, Bilateral Crus I, Crus I Left, Crus I Right	Fig 2 S2D (left), Fig 3 S1A-B
CNO only, Vehicle only, mCherry, Untreated only		Fig 3 S1C
CNO only no reversal	Lobule VI no reversal	Figure 3 S1D
Untreated only	Lobule VI, Bilateral Crus I, Crus I Left, Crus I Right	Figure 3 S1E
CNO only	Lobule VI, Crus I Right	Figure 3 S1F
Acquisition, Habituation, CNO only	Crus I Left, Crus I Right	Figure 5 S1
Acquisition, Habituation		Figure 6 S1 A-C
Acquisition, Habituation, CNO only, CNO no reversal	Lobule VI	Figure 6 S2

Table supplement 1: Control and experimental conditions per figure.

Additional supplementary items

1) Movie S1. Semi-supervised behavioral classification. Example movie of mouse in open field (left), zoomed-in version with LEAP labels (middle) and corresponding ethogram (right).
2) Movie S2. Y-maze task. Example movie of mouse performing Y-maze acquisition, reversal with CNO only, and lobule VI perturbed mouse attempting reversal.
3) Movie S3. Whole brain lightsheet. Example movie of a cleared brain using iDISCO+, c-Fos staining, clearmap cell counts, and neuroglancer overlay of multiple thalamic regions.
4) Data S1. Effects of experimental perturbations on c-Fos cell counts. Contrasts include acquisition versus habituation, reversal learning versus acquisition, and lobule VI perturbation via DREADDs against CNO only. For each brain region and contrast, negative binomial (NB) regression was performed with natural log of total counts across all regions as an offset. Estimate: NB slope coefficient for effect of treatment (log-ratio scale), Fold change: exponentiated coefficient (ratio scale), Std. Error: standard error of estimate, z value: estimate divided by standard error (also known as effect size), Pr(>|z|): raw p-value for effect, fdr_adj_pval: p-value adjusted for false discovery rate, status: whether NB fitting routine encountered numerical problems.

References

Andersson G, Oscarsson O. 1978. Climbing fiber microzones in cerebellar vermis and their projection to different groups of cells in the lateral vestibular nucleus. *Exp Brain Res* **32**:565–579.

Andres KH, von Düring M, Veh RW. 1999. Subnuclear organization of the rat habenular complexes. *J Comp Neurol* **407**:130–150.

Apps R, Hawkes R. 2009. Cerebellar cortical organization: a one-map hypothesis. *Nat Rev Neurosci* **10**:670–681.

Badura A, Verpeut JL, Metzger JW, Pereira TD. 2018. Normal cognitive and social development require posterior cerebellar activity. *Elife*.

Bates D, Mächler M, Bolker B, Walker S. 2015. Fitting Linear Mixed-Effects Models Using lme4. *Journal of Statistical Software, Articles* **67**:1–48.

Benjamini Y, Hochberg Y. 1995. Controlling the false discovery rate: A practical and powerful approach to multiple testing. *J R Stat Soc* **57**:289–300.

Boulougouris V, Dalley JW, Robbins TW. 2007. Effects of orbitofrontal, infralimbic and prelimbic cortical lesions on serial spatial reversal learning in the rat. *Behav Brain Res* **179**:219–228.

Burton H, Jones EG. 1976. The posterior thalamic region and its cortical projection in New World and Old World monkeys. *J Comp Neurol* **168**:249–301.

Capuzzo G, Floresco SB. 2020. Prelimbic and Infralimbic Prefrontal Regulation of Active and Inhibitory Avoidance and Reward-Seeking. *J Neurosci* **40**:4773–4787.

Caulfield MD, Zhu DC, McAuley JD, Servatius RJ. 2016. Individual differences in resting-state functional connectivity with the executive network: support for a cerebellar role in anxiety vulnerability. *Brain Struct Funct* **221**:3081–3093.

Cavdar S, Onat FY, Yananli HR, Sehirli US, Tulay C, Saka E, Gürdal E. 2002. Cerebellar connections to the rostral reticular nucleus of the thalamus in the rat. *J Anat* **201**:485–491.

Chao OY, Pathak SS, Zhang H, Augustine G, Christie J, Kikuchi C, Taniguchi H, Yang Y-M. 2022. Social memory deficit gated by dysregulation of the cerebellar vermis. doi:10.21203/rs.3.rs-1393639/v1

Chiang MC, Bowen A, Schier LA, Tupone D, Uddin O, Heinricher MM. 2019. Parabrachial Complex: A Hub for Pain and Aversion. *J Neurosci* **39**:8225–8230.

Crucitti J, Hyde C, Enticott PG, Stokes MA. 2020. Are Vermal Lobules VI-VII Smaller in Autism Spectrum Disorder? *Cerebellum* **19**:617–628.

Deng H, Xiao X, Wang Z. 2016. Periaqueductal Gray Neuronal Activities Underlie Different Aspects of Defensive Behaviors. *J Neurosci* **36**:7580–7588.

Deverett B, Kislin M, Tank DW, Wang SS-H. 2019. Cerebellar disruption impairs working memory during evidence accumulation. *Nat Commun* **10**:3128.

Deverett B, Koay SA, Oostland M, Wang SS-H. 2018. Cerebellar involvement in an evidence-accumulation decision-making task. *eLife*. doi:10.7554/elife.36781

De Zeeuw CI. 2021. Bidirectional learning in upbound and downbound microzones of the cerebellum. *Nat Rev Neurosci* **22**:92–110.

De Zeeuw CI, Lisberger SG, Raymond JL. 2021. Publisher Correction: Diversity and dynamism in the cerebellum. *Nat Neurosci* **24**:450.

Dragunow M, Faull R. 1989. The use of c-fos as a metabolic marker in neuronal pathway tracing. *J Neurosci Methods* **29**:261–265.

Eccles JC, Llinás R, Sasaki K. 1966. The excitatory synaptic action of climbing fibres on the Purkinje cells of the cerebellum. *J Physiol* **182**:268–296.

Fatemi SH, Aldinger KA, Ashwood P, Bauman ML, Blaha CD, Blatt GJ, Chauhan A, Chauhan V, Dager SR, Dickson PE, Estes AM, Goldowitz D, Heck DH, Kemper TL, King BH, Martin LA, Millen KJ, Mittleman G, Mosconi MW, Persico AM, Sweeney JA, Webb SJ, Welsh JP. 2012. Consensus paper: pathological role of the cerebellum in autism. *Cerebellum* **11**:777–

807.
Fields RD, Eshete F, Stevens B, Itoh K. 1997. Action potential-dependent regulation of gene expression: temporal specificity in ca2+, cAMP-responsive element binding proteins, and mitogen-activated protein kinase signaling. *J Neurosci* **17**:7252–7266.
Fujita H, Kodama T, du Lac S. 2020. Modular output circuits of the fastigial nucleus for diverse motor and nonmotor functions of the cerebellar vermis. *Elife* **9**. doi:10.7554/eLife.58613
Fuller PM, Sherman D, Pedersen NP, Saper CB, Lu J. 2011. Reassessment of the structural basis of the ascending arousal system. *J Comp Neurol* **519**:933–956.
Ghahremani DG, Monterosso J, Jentsch JD, Bilder RM, Poldrack RA. 2010. Neural components underlying behavioral flexibility in human reversal learning. *Cereb Cortex* **20**:1843–1852.
Giovannucci A, Badura A, Deverett B, Najafi F, Pereira TD, Gao Z, Ozden I, Kloth AD, Pnevmatikakis E, Paninski L, De Zeeuw CI, Medina JF, Wang SS-H. 2017. Cerebellar granule cells acquire a widespread predictive feedback signal during motor learning. *Nat Neurosci* **20**:727–734.
Gomez JL, Bonaventura J, Lesniak W, Mathews WB, Sysa-Shah P, Rodriguez LA, Ellis RJ, Richie CT, Harvey BK, Dannals RF, Pomper MG, Bonci A, Michaelides M. 2017. Chemogenetics revealed: DREADD occupancy and activation via converted clozapine. *Science* **357**:503–507.
Gravel C, Hawkes R. 1990. Parasagittal organization of the rat cerebellar cortex: direct comparison of Purkinje cell compartments and the organization of the spinocerebellar projection. *J Comp Neurol* **291**:79–102.
Guillery RW, Harting JK. 2003. Structure and connections of the thalamic reticular nucleus: Advancing views over half a century. *J Comp Neurol* **463**:360–371.
Halassa MM, Kastner S. 2017. Thalamic functions in distributed cognitive control. *Nat Neurosci* **20**:1669–1679.
Harting JK, Van Lieshout DP, Feig S. 1991. Connectional studies of the primate lateral geniculate nucleus: distribution of axons arising from the thalamic reticular nucleus of Galago crassicaudatus. *J Comp Neurol* **310**:411–427.
Hothorn T, Bretz F, Westfall P. 2008. Simultaneous inference in general parametric models. *Biom J* **50**:346–363.
Houser CR, Vaughn JE, Barber RP, Roberts E. 1980. GABA neurons are the major cell type of the nucleus reticularis thalami. *Brain Res* **200**:341–354.
Hu H, Cui Y, Yang Y. 2020. Circuits and functions of the lateral habenula in health and in disease. *Nat Rev Neurosci* **21**:277–295.
Jendryka M, Palchaudhuri M, Ursu D, van der Veen B, Liss B, Kätzel D, Nissen W, Pekcec A. 2019. Pharmacokinetic and pharmacodynamic actions of clozapine-N-oxide, clozapine, and compound 21 in DREADD-based chemogenetics in mice. *Sci Rep* **9**:4522.
Jones EG. 2012. The Thalamus. Springer Science & Business Media.
Jun JJ, Steinmetz NA, Siegle JH, Denman DJ, Bauza M, Barbarits B, Lee AK, Anastassiou CA, Andrei A, Aydın Ç, Barbic M, Blanche TJ, Bonin V, Couto J, Dutta B, Gratiy SL, Gutnisky DA, Häusser M, Karsh B, Ledochowitsch P, Lopez CM, Mitelut C, Musa S, Okun M, Pachitariu M, Putzeys J, Rich PD, Rossant C, Sun W-L, Svoboda K, Carandini M, Harris KD, Koch C, O'Keefe J, Harris TD. 2017. Fully integrated silicon probes for high-density recording of neural activity. *Nature* **551**:232–236.
Kelly E, Meng F, Fujita H, Morgado F, Kazemi Y, Rice LC, Ren C, Escamilla CO, Gibson JM, Sajadi S, Pendry RJ, Tan T, Ellegood J, Basson MA, Blakely RD, Dindot SV, Golzio C, Hahn MK, Katsanis N, Robins DM, Silverman JL, Singh KK, Wevrick R, Taylor MJ, Hammill C, Anagnostou E, Pfeiffer BE, Stoodley CJ, Lerch JP, du Lac S, Tsai PT. 2020. Regulation of autism-relevant behaviors by cerebellar-prefrontal cortical circuits. *Nat Neurosci* **23**:1102–1110.
Kelly RM, Strick PL. 2003. Cerebellar loops with motor cortex and prefrontal cortex of a

nonhuman primate. *J Neurosci* **23**:8432–8444.
Klibaite U, Kislin M, Verpeut JL, Bergeler S, Sun X, Shaevitz JW, Wang SS-H. 2022. Deep phenotyping reveals movement phenotypes in mouse neurodevelopmental models. *Mol Autism* **13**:12.
Kloth AD, Badura A, Li A, Cherskov A, Connolly SG, Giovannucci A, Ali Bangash M, Grasselli G, Peñagarikano O, Piochon C, Tsai PT, Geschwind DH, Hansel C, Sahin M, Takumi T, Worley PF, Wang SS-H. 2015. Cerebellar associative sensory learning defects in five mouse autism models. *eLife*. doi:10.7554/elife.06085
Latinus M, Cléry H, Andersson F, Bonnet-Brilhault F, Fonlupt P, Gomot M. 2019. Inflexibility in Autism Spectrum Disorder: Need for certainty and atypical emotion processing share the blame. *Brain Cogn* **136**:103599.
Leiner HC, Leiner AL, Dow RS. 1993. Cognitive and language functions of the human cerebellum. *Trends Neurosci* **16**:444–447.
Leiner HC, Leiner AL, Dow RS. 1986. Does the cerebellum contribute to mental skills? *Behav Neurosci* **100**:443–454.
Limperopoulos C, Chilingaryan G, Guizard N, Robertson RL, Du Plessis AJ. 2010. Cerebellar Injury in the Premature Infant Is Associated With Impaired Growth of Specific Cerebral Regions. *Pediatr Res* **68**:145–150.
Limperopoulos C, Chilingaryan G, Sullivan N, Guizard N, Robertson RL, Du Plessis AJ. 2014. Injury to the premature cerebellum: outcome is related to remote cortical development. *Cereb Cortex* **24**:728–736.
Machado AS, Darmohray DM, Fayad J, Marques HG, Carey MR. 2015. A quantitative framework for whole-body coordination reveals specific deficits in freely walking ataxic mice. *Elife* **4**. doi:10.7554/eLife.07892
Maes JHR, Eling PATM, Wezenberg E, Vissers CTWM, Kan CC. 2011. Attentional set shifting in autism spectrum disorder: differentiating between the role of perseveration, learned irrelevance, and novelty processing. *J Clin Exp Neuropsychol* **33**:210–217.
Manvich DF, Webster KA, Foster SL, Farrell MS, Ritchie JC, Porter JH, Weinshenker D. 2018. The DREADD agonist clozapine N-oxide (CNO) is reverse-metabolized to clozapine and produces clozapine-like interoceptive stimulus effects in rats and mice. *Sci Rep* **8**:3840.
Martín Fernández JA, Daunis i Estadella J, Mateu i Figueras G. 2015. On the interpretation of differences between groups for compositional data. *SORT: statistics and operations research transactions, 2015, vol 39, núm 2, p 231-252*.
Mathis A, Mamidanna P, Cury KM, Abe T, Murthy VN, Mathis MW, Bethge M. 2018. DeepLabCut: markerless pose estimation of user-defined body parts with deep learning. *Nat Neurosci* **21**:1281–1289.
Nath T, Mathis A, Chen AC, Patel A, Bethge M, Mathis MW. 2019. Using DeepLabCut for 3D markerless pose estimation across species and behaviors. *Nat Protoc* **14**:2152–2176.
Ottaviani C, Watson DR, Meeten F, Makovac E, Garfinkel SN, Critchley HD. 2016. Neurobiological substrates of cognitive rigidity and autonomic inflexibility in generalized anxiety disorder. *Biol Psychol* **119**:31–41.
Ozaki K, Ohnishi Y, Iida A, Sekine A, Yamada R, Tsunoda T, Sato H, Sato H, Hori M, Nakamura Y, Tanaka T. 2002. Functional SNPs in the lymphotoxin-α gene that are associated with susceptibility to myocardial infarction. *Nat Genet* **32**:650–654.
Ozol K, Hayden JM, Oberdick J, Hawkes R. 1999. Transverse zones in the vermis of the mouse cerebellum. *J Comp Neurol* **412**:95–111.
Pereira TD, Aldarondo DE, Willmore L, Kislin M, -H. Wang SS, Murthy M, Shaevitz JW. 2019. Fast animal pose estimation using deep neural networks. *Nature Methods* **16**:117–125.
Pereira TD, Tabris N, Matsliah A, Turner DM, Li J, Ravindranath S, Papadoyannis ES, Normand E, Deutsch DS, Wang ZY, McKenzie-Smith GC, Mitelut CC, Castro MD, D'Uva J, Kislin M, Sanes DH, Kocher SD, Wang SS-H, Falkner AL, Shaevitz JW, Murthy M. 2022. SLEAP: A

deep learning system for multi-animal pose tracking. *Nat Methods* **19**:486–495.
Pisano TJ, Dhanerawala ZM, Kislin M, Bakshinskaya D, Engel EA, Hansen EJ, Hoag AT, Lee J, de Oude NL, Venkataraju KU, Verpeut JL, Hoebeek FE, Richardson BD, Boele H-J, Wang SS-H. 2021. Homologous organization of cerebellar pathways to sensory, motor, and associative forebrain. *Cell Rep* **36**:109721.
Pisano TJ, Hoag AT, Dhanerawala ZM, Guariglia SR, Jung C, Boele H-J, Seagraves KM, Verpeut JL, Wang SS-H. 2022. Automated high-throughput mouse transsynaptic viral tracing using iDISCO+ tissue clearing, light-sheet microscopy, and BrainPipe. *STAR Protocols* **3**:101289.
Reeber SL, White JJ, George-Jones NA, Sillitoe RV. 2012. Architecture and development of olivocerebellar circuit topography. *Front Neural Circuits* **6**:115.
Reese RM, Richman DM, Zarcone J, Zarcone T. 2003. Individualizing Functional Assessments for Children with Autism: The Contribution of Perseverative Behavior and Sensory Disturbances to Disruptive Behavior. *Focus Autism Other Dev Disabl* **18**:89–94.
Renier N, Adams EL, Kirst C, Wu Z, Azevedo R, Kohl J, Autry AE, Kadiri L, Umadevi Venkataraju K, Zhou Y, Wang VX, Tang CY, Olsen O, Dulac C, Osten P, Tessier-Lavigne M. 2016. Mapping of Brain Activity by Automated Volume Analysis of Immediate Early Genes. *Cell* **165**:1789–1802.
Renier N, Wu Z, Simon DJ, Yang J, Ariel P, Tessier-Lavigne M. 2014. iDISCO: a simple, rapid method to immunolabel large tissue samples for volume imaging. *Cell* **159**:896–910.
Saper CB. 2000. Hypothalamic connections with the cerebral cortexProgress in Brain Research. Elsevier. pp. 39–48.
Sasson NJ, Turner-Brown LM, Holtzclaw TN, Lam KSL, Bodfish JW. 2008. Children with autism demonstrate circumscribed attention during passive viewing of complex social and nonsocial picture arrays. *Autism Res* **1**:31–42.
Schmahmann JD. 2013. Cerebellar Cognitive Affective Syndrome and the Neuropsychiatry of the Cerebellum. *Handbook of the Cerebellum and Cerebellar Disorders*. doi:10.1007/978-94-007-1333-8_77
Schmahmann JD. 2004. Disorders of the cerebellum: ataxia, dysmetria of thought, and the cerebellar cognitive affective syndrome. *J Neuropsychiatry Clin Neurosci* **16**:367–378.
Schmahmann JD, Sherman JC. 1998. The cerebellar cognitive affective syndrome. *Brain* **121 (Pt 4)**:561–579.
Sillitoe RV, Künzle H, Hawkes R. 2003. Zebrin II compartmentation of the cerebellum in a basal insectivore, the Madagascan hedgehog tenrec Echinops telfairi. *J Anat* **203**:283–296.
Steinmetz NA, Aydin C, Lebedeva A, Okun M, Pachitariu M, Bauza M, Beau M, Bhagat J, Böhm C, Broux M, Chen S, Colonell J, Gardner RJ, Karsh B, Kloosterman F, Kostadinov D, Mora-Lopez C, O'Callaghan J, Park J, Putzeys J, Sauerbrei B, van Daal RJJ, Vollan AZ, Wang S, Welkenhuysen M, Ye Z, Dudman JT, Dutta B, Hantman AW, Harris KD, Lee AK, Moser EI, O'Keefe J, Renart A, Svoboda K, Häusser M, Haesler S, Carandini M, Harris TD. 2021. Neuropixels 2.0: A miniaturized high-density probe for stable, long-term brain recordings. *Science* **372**. doi:10.1126/science.abf4588
Stoodley CJ, D'Mello AM, Ellegood J, Jakkamsetti V, Liu P, Nebel MB, Gibson JM, Kelly E, Meng F, Cano CA, Pascual JM, Mostofsky SH, Lerch JP, Tsai PT. 2017. Altered cerebellar connectivity in autism and cerebellar-mediated rescue of autism-related behaviors in mice. *Nat Neurosci* **20**:1744–1751.
Strick PL, Dum RP, Fiez JA. 2009. Cerebellum and nonmotor function. *Annu Rev Neurosci* **32**:413–434.
Traut N, Beggiato A, Bourgeron T, Delorme R, Rondi-Reig L, Paradis A-L, Toro R. 2018. Cerebellar Volume in Autism: Literature Meta-analysis and Analysis of the Autism Brain Imaging Data Exchange Cohort. *Biol Psychiatry* **83**:579–588.
Tsai PT, Hull C, Chu Y, Greene-Colozzi E, Sadowski AR, Leech JM, Steinberg J, Crawley JN,

Regehr WG, Sahin M. 2012. Autistic-like behaviour and cerebellar dysfunction in Purkinje cell Tsc1 mutant mice. *Nature* **488**:647–651.
Tsai PT, Rudolph S, Guo C, Ellegood J, Gibson JM, Schaeffer SM, Mogavero J, Lerch JP, Regehr W, Sahin M. 2018. Sensitive Periods for Cerebellar-Mediated Autistic-like Behaviors. *Cell Rep* **25**:357–367.e4.
Uddin LQ, Supekar K, Lynch CJ, Cheng KM, Odriozola P, Barth ME, Phillips J, Feinstein C, Abrams DA, Menon V. 2015. Brain State Differentiation and Behavioral Inflexibility in Autism. *Cereb Cortex* **25**:4740–4747.
Vanderwolf CH, Stewart DJ. 1988. Thalamic control of neocortical activation: a critical re-evaluation. *Brain Res Bull* **20**:529–538.
Venables WN, Ripley BD. 2002. Modern Applied Statistics with S. *Statistics and Computing*. doi:10.1007/978-0-387-21706-2
Wang SS-H, Kloth AD, Badura A. 2014. The cerebellum, sensitive periods, and autism. *Neuron* **83**:518–532.
Wiltschko AB, Johnson MJ, Iurilli G, Peterson RE, Katon JM, Pashkovski SL, Abraira VE, Adams RP, Datta SR. 2015. Mapping Sub-Second Structure in Mouse Behavior. *Neuron* **88**:1121–1135.
Wiltschko AB, Tsukahara T, Zeine A, Anyoha R, Gillis WF, Markowitz JE, Peterson RE, Katon J, Johnson MJ, Datta SR. 2020. Revealing the structure of pharmacobehavioral space through motion sequencing. *Nat Neurosci*. doi:10.1038/s41593-020-00706-3